creative commons
COMMONS DEED

저작자표시-비영리-동일조건변경허락 2.0 대한민국

이용자는 아래의 조건을 따르는 경우에 한하여 자유롭게

- 이 저작물을 복제, 배포, 전송, 전시, 공연 및 방송할 수 있습니다.
- 이차적 저작물을 작성할 수 있습니다.

다음과 같은 조건을 따라야 합니다:

저작자표시. 귀하는 원저작자를 표시하여야 합니다.

비영리. 귀하는 이 저작물을 영리 목적으로 이용할 수 없습니다.

동일조건변경허락. 귀하가 이 저작물을 개작, 변형 또는 가공했을 경우에는, 이 저작물과 동일한 이용허락조건하에서만 배포할 수 있습니다.

- 귀하는, 이 저작물의 재이용이나 배포의 경우, 이 저작물에 적용된 이용허락조건을 명확하게 나타내어야 합니다.
- 저작권자로부터 별도의 허가를 받으면 이러한 조건들은 적용되지 않습니다.

저작권법에 따른 이용자의 권리는 위의 내용에 의하여 영향을 받지 않습니다.

이것은 이용허락규약(Legal Code)을 이해하기 쉽게 요약한 것입니다.

Disclaimer

dCollection

공학박사 학위논문

Effects of Catalyst Surface Structure on Electrochemical Property and Catalytic Activity in Fuel Cell

연료전지 촉매의 표면 구조 변화로 인한
전기화학적 성질 및 촉매 활성에 미치는 영향

2012년 8월

서울대학교 대학원
공과대학 화학생물공학부

정 남 기

Abstract

Effects of Catalyst Surface Structure on Electrochemical Property and Catalytic Activity in Fuel Cell

Namgee Jung

School of Chemical & Biological Engineering

Seoul National University

Proton exchange membrane fuel cell (PEMFC) has been intensively studied since it has a large potential as the electrochemical energy conversion device for the future. It is much more efficient than a combustion engine because it can directly convert the chemical energy to the electricity without any mechanical process. However, there are still lots of unsolved problems for the commercialization. Those problems are complicatedly connected with material development, device fabrication process, operation conditions, and fuel reforming and storage, but the most important part in PEMFC is the membrane electrode assembly (MEA), in which the electricity is produced through the electrochemical reactions. Especially, one of the main key for the enhanced performance of PEMFC is a cathode electrode of the MEA. In PEMFC, two large overpotential losses are occurred in the cathode. One is related to the charge transfer resistance for the sluggish oxygen reduction reaction (ORR) in a low current density region. To decrease the charge transfer resistance, the developments of metal nanoparticles have been conducted through PtM (M = Fe, Co, Ni) alloying, core-shell structure, and shape control. The other one is induced by the mass transfer resistance due to

water flooding in a high current density region in the MEA cathode. Water produced by the ORR in the cathode is accumulated on carbon support and between catalyst agglomerates, which results in blocking the oxygen transfer to the catalyst surface in the MEA cathode. To improve the water management in the MEA cathode, the insertion of hydrophobic particle or pore forming agent into the cathode catalyst layer has been performed. However, these two overpotentials still mainly affect the PEMFC performance degradation despite the efforts.

It is considered that the catalyst surfaces (metal nanoparticle and carbon support) are the critical factors to solve the problems since both the ORR on nanoparticle and water accumulation on carbon support are directly related to the material surface property. Firstly, to develop the cathode catalyst with high ORR activity, a carbon-supported PtNi alloy (PtNi/C) catalyst was synthesized, and the surface structural effects were investigated thorough various surface modifications of PtNi/C in this thesis. The surface Ni atoms were leached out from as-prepared PtNi/C by the acid treatment, and de-alloyed PtNi/C was fabricated. In addition, the acid-treated PtNi/C was then heated to make the de-alloyed PtNi/C with a smooth surface structure. Furthermore, Pt atoms were additionally deposited on the acid-treated PtNi/C and acid/heat-treated PtNi/C, respectively, and the effects of the surface structure of substrate materials on additional Pt overlayers were identified. The change of surface structures was mainly studied by the CO oxidation current measurement. In addition, the effect of surface modifications on Pt electronic structure was confirmed by the X-ray absorption near-edge structure (XANES) spectroscopy and potential of zero total charge (PZTC) measurements. The degree of formation of (111) and (100) facets was different according to the surface modification process, and it caused the different Pt electronic structures and electrochemical surface properties in the catalysts. Therefore, the binding energy between Pt and oxygenated species

was changed by the surface structure modifications, which resulted in distinct differences of the ORR activities of the catalysts.

Secondly, to enhance the water transport in the MEA cathode, the carbon surface in carbon-supported Pt (Pt/C) catalyst was selectively functionalized using a thermally responsive poly(N-isopropylacrylamide) (PNIPAM). In general, a carbon support has a hydrophilic property since the functional groups on carbon surface are needed to load metal nanoparticles on the surfaces, and the hydrophilic carbon surface is also required to be well mixed with other components, which are Nafion ionomer, water, and alcohol solvent, in the catalyst ink when the MEA fabricated. However, after the MEA fabrication, a hydrophobic property of the carbon is necessary to prevent from the water accumulation on the carbon surface at ~70 °C in the PEMFC operation. To solve these requirements for the carbon surface properties, PNIPAM-functionalized Pt/C (Pt/C-PNIPAM) was fabricated, and the functionalization process hardly affected Pt surface. The selective carbon functionalization was identified by X-ray photoelectron spectroscopy (XPS) and cyclic voltammetry (CV). The thermal responsibility was confirmed by the contact angle (CA) hysteresis measurement between 20 and 70 °C. Through the selective carbon surface modification, Pt/C-PNIPAM was well dispersed in the catalyst ink without any problem when the catalyst ink prepared, and the PEMFC performance was increased due to the enhanced water transport at 70 °C in the PEMFC operation. In addition, the relation between the modified carbon surface and water was understood by a simple theoretical modeling.

These surface modifications of fuel cell catalysts (metal nanoparticle and carbon support) could give significant changes of the electrochemical property and catalytic activity in PEMFC. In addition, the strategies for advanced material designs in the electrochemical energy conversion devices could be obtained by understanding various catalyst surface structures.

***Keywords*:** fuel cell, catalyst, carbon, surface structure, oxygen reduction reaction, water transport
***Student Number*:** 2009-31264

Contents

Chapter 1. Introduction 1

1.1. Fuel cell basics 1

1.1.1. Fuel cells as electrochemical energy conversion device 1

1.1.2. Proton exchange membrane fuel cell (PEMFC) 5

1.2. Development of fuel cell catalysts 12

1.2.1. Fuel cell catalysts 12

1.2.2. Oxygen reduction reaction (ORR) in PEMFC cathode 15

1.2.3. Water management in PEMFC cathode 19

1.3. References 22

Chapter 2. Experimental 30

2.1. Surface modification of PtNi alloy catalyst 30

2.1.1. Preparation of carbon-supported PtNi alloy catalyst 30

2.1.2. Surface structure modifications of PtNi alloy catalyst 30

2.2. Surface modification of carbon support 32

2.2.1. Selective functionalization of carbon-supported Pt catalyst 32

2.2.2. Membrane electrode assembly (MEA) fabrication 32

2.3. Electrochemical characterization 35

2.4. Physical and electronic structure measurements 38

2.5. References 42

Chapter 3. Results and Discussion 44

3.1. Effects of surface structure of core material on Pt over layer 44

3.1.1. Effects of surface structure of de-alloyed PtNi catalysts 44

3.1.2. Effects of de-alloyed PtNi catalyst on Pt overlayer 59

3.2. Effects of carbon surface modification 73

3.2.1. Selective functionalization of carbon support 73

3.2.2. Thermal responsibility of modified carbon surface 86

3.2.3. Enhanced water transport in cathode of PEMFC 89

3.3. References 95

Chapter 4. Conclusions 100

국 문 초 록 105

List of Tables

Table 1.1 Types of fuel cells 3
Table 3.1 Physical properties of PtNi/C-ASP, PtNi/C-acid, and PtNi/C-acid/heat obtained from ICP-AES, EA, and XRD 50
Table 3.2 Physical properties of Pt@PtNi/C-acid and Pt@PtNi/C-acid/heat obtained from ICP-AES, EA, and XRD..... 64
Table 3.3 Atomic ratio of Pt oxidation states of Pt/C and Pt/C-PNIPAM . 84
Table 3.4 Contact angle (static, advancing and receding) data depending on temperature and surface composing materials. Hysteresis in the adhesion energy was calculated based on the data..... 88

List of Figures

Fig. 1.1 Application fields of fuel cells 4
Fig. 1.2 Anode and cathode reactions in PEMFC 7
Fig. 1.3 Principle of PEMFC operation 8
Fig. 1.4 Components of membrane electrode assembly (MEA) 9
Fig. 1.5 Schematic diagram of tri-phase boundary in fuel cell 10
Fig. 1.6 Potential losses in fuel cell polarization curve 11
Fig. 1.7 Components of PEMFC catalyst 14
Fig. 1.8 *d*-band center and 4f core-level downshift by PtNi alloying 18
Fig. 1.9 Water flooding in carbon surface and catalyst agglomerates 21
Fig. 2.1 Components of unit cell 34
Fig. 2.2 Equivalent circuit of PEMFC. (L: inductance of wire, Rs: series resistance, Rct: charge transfer resistance, CPE: constant phase element, W: Warbug impedance) 37
Fig. 2.3 Pohang light source (PLS) beam status. From the web page, http://pal.postech.ac.kr 41
Fig. 3.1 TEM images of (a) PtNi/C-ASP, (b) PtNi/C-acid, and (c) PtNi/C-acid/heat 51
Fig. 3.2 XRD patterns of PtNi/C-ASP, PtNi/C-acid, and PtNi/C-acid/heat 52
Fig. 3.3 Schematic representation that summarizes the four CO oxidation current peaks and assigns them to specific surface domains and sites 53
Fig. 3.4 (a) CO oxidation currents and (b) first derivative of CO oxidation currents of PtNi/C-ASP, PtNi/C-acid, and PtNi/C-acid/heat 54
Fig. 3.5 XANES spectra of (a) Pt L_{III} edge and (b) Ni K edge for PtNi/C-ASP, PtNi/C-acid, and PtNi/C-acid/heat 55

Fig. 3.6 N_2O reduction currents for PtNi/C-ASP, PtNi/C-acid, and PtNi/C-acid/heat 56
Fig. 3.7 CVs of PtNi/C-acid and PtNi/C-acid heat in 0.1 M $HClO_4$ 57
Fig. 3.8 ORR curves for PtNi/C-acid and PtNi/C-acid/heat in 0.1 M $HClO_4$ 58
Fig. 3.9 TEM images of Pt@PtNi/C-acid with (a) low magnification and (b) high magnification 65
Fig. 3.10 TEM images of Pt@PtNi/C-acid with (a) low magnification and (b) high magnificationrations 66
Fig. 3.11 XRD patterns of Pt@PtNi/C-acid and Pt@PtNi/C-acid/heat 67
Fig. 3.12 (a) CO oxidation currents and (b) first derivative of CO oxidation currents of Pt@PtNi/C-acid and Pt@PtNi/C-acid/heat 68
Fig. 3.13 XANES spectra of (a) Pt L_{III} edge and (b) Ni K edge for Pt@PtNi/C-acid and Pt@PtNi/C-acid/heat 69
Fig. 3.14 N_2O reduction currents for Pt@PtNi/C-acid and Pt@PtNi/C-acid/heat 70
Fig. 3.15 CVs of Pt@PtNi/C-acid and Pt@PtNi/C-acid heat in 0.1 M $HClO_4$ 71
Fig. 3.16 ORR curves for Pt@PtNi/C-acid and Pt@PtNi/C-acid/heat in 0.1 M $HClO_4$ 72
Fig. 3.17 Schematic illustration of synthesis of selectively-functionalized Pt/C (Pt/C-PNIPAM) 78
Fig. 3.18 SEM images showing the catalyst layer thickness of (a) Pt/C (~4.9 μm) and (b) Pt/C-PNIPAM (~5.0 μm) 79
Fig. 3.19 AFM images showing the morphology of each surface: (a) Pt/C, (b) Pt/C-PNIPAM. Each inset shows corresponding SEM images. (Scale bar: 50 nm) 80
Fig. 3.20 XPS peaks of N1s for Pt/C and Pt/C-PNIPAM 81
Fig. 3.21 (a) XPS peaks of Pt4f and (b) CVs for Pt/C and Pt/C-PNIPAM .. 82

Fig. 3.22 Deconvolution for XPS peaks of Pt4f of (a) Pt/C and (b) Pt/C-PNIPAM 83
Fig. 3.23 XRD patterns for Pt/C and Pt/C-PNIPAM..... 85
Fig. 3.24 Photographs of advancing and receding contact angles depending on temperature and surface material 87
Fig. 3.25 Unit cell performance of MEAs with Pt/C and Pt/C-PNIPAM.... 93
Fig. 3.26 EIS of MEAs with Pt/C and Pt/C-PNIPAM. (Dot: raw data, Line: fitting data) 94

Chapter 1. Introduction

1.1. Fuel cell basics

1.1.1. Fuel cells as electrochemical energy conversion device

Fuel cell is an electrochemical device that converts chemical energy of fuel into electricity without any mechanical process, meaning no moving parts. Since fuel cell produces the electricity directly from chemical energy, it is far more efficient than combustion engine. In addition, fuel cell emits no undesirable products such as NO_x, SO_x, and particulates [1].

As the electrochemical energy conversion device, fuel cell is similar to battery because it has the anode and cathode electrodes and electrolyte, and generates electricity through electrochemical reactions. However, while battery should be recharged for a long time after it is fully discharged, fuel cell can produce the electricity continuously as long as fuel is supplied into the electrode. In addition, various fuels such as H_2, natural gas, and liquid alcohol can be used in the different type of fuel cells according to the applications [2]. Due to the advantages, fuel cell is intensively studied as an alternative energy device to replace the gasoline engine for the future.

As shown in Table 1.1, fuel cells are classified according to the types of electrolyte. The mobile ions and operating temperatures are different due to the characteristic of electrolytes.

(1) Proton exchange membrane fuel cell (PEMFC)

(2) Phosphoric acid fuel cell (PAFC)

(3) Alkaline fuel cell (AFC)

(4) Molten carbonate fuel cell (MCFC)

(5) Solid oxide fuel cell (SOFC)

As the operating temperature is high, low price catalysts such as Ni can be used because the activation energy of reactants becomes decreased. In addition, many types of fuel can be available, for examples, natural gas and CO gas, since the effect of Pt poisoning by CO is reduced in high temperature. However, in fuel cells operated below 200 °C, precious Pt catalyst is needed to obtain a high catalytic activity. As shown in Fig. 1.1, MCFC and SOFC are generally utilized for the power plant since high temperature is required, but PEMFC is developed for vehicle engine and mobile applications due to low operating temperature and rapid response ability.

Table 1.1 Types of fuel cells.

	PEMFC	PAFC	AFC	MCFC	SOFC
Electrolyte	Proton Exchange Polymer	Liquid H_3PO_4 (Immobilized)	Anion Exchange Polymer	Molten Carbonate	YSZ (Ceramic)
Charge Carrier	H^+	H^+	OH^-	CO_3^{2-}	O^{2-}
Operating Temperature	80 °C	200 °C	60 - 220 °C	650 °C	600 - 1000 °C
Catalyst	Pt	Pt	Pt	Ni	Ni/YSZ, LSM
Fuel	H_2 & alcohol	H_2	H_2	H_2 & CH_4	H_2, CH_4 & CO

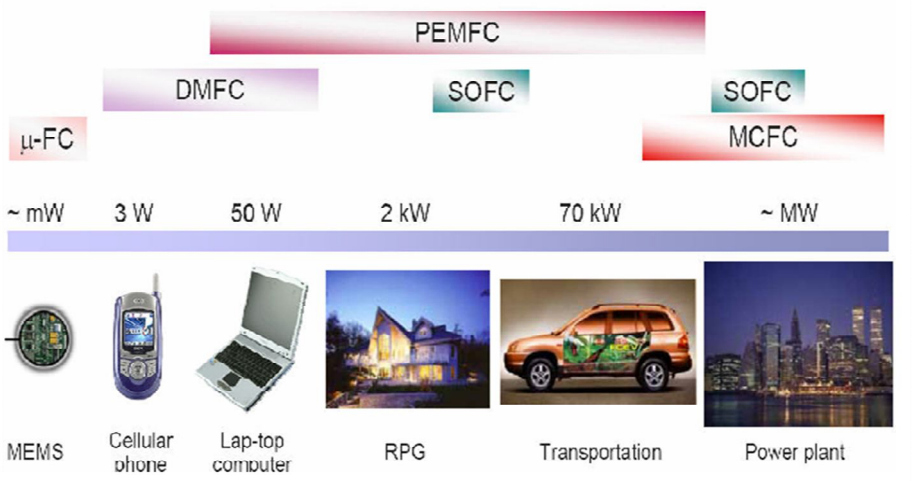

Fig. 1.1 Application fields of fuel cells.

1.1.2. Proton exchange membrane fuel cell (PEMFC)

PEMFC shows a lot of applications which are portable power, vehicle engine, and residential power generation (RPG) because it can cover various electric power and working voltages as shown in Fig. 1.1. H_2 is typically used as a fuel in PEMFC due to its low activation energy and rapid reaction rate for the hydrogen oxidation reaction (HOR). However, direct methanol fuel cell (DMFC) using liquid methanol as a fuel, one of the PEMFC, is mainly applied to the portable devices due to its low power density. In PEMFC using H_2, involved electrochemical reactions are the HOR and oxygen reduction reaction (ORR) in the anode and cathode, respectively (Fig. 1.2). A theoretical voltage and efficiency are 1.229 V and 83 %, respectively. As shown in Fig. 1.3, H_2 and O_2 are flowed into the PEMFC, and the electrons and water are produced.

A membrane electrode assembly (MEA) in PEMFC is the most important component in PEMFC system due to the part producing electricity. As shown in Fig. 1.4, it is composed of the anode and cathode catalyst layers, polymer membrane, and two gas diffusion layers (GDL). Highly dispersed noanoparticles on carbon support is properly distributed in the anode and cathode catalyst layers. The polymer membrane should be thin enough to help protons flow easily from the anode to cathode, and the GDL has high porosity and electron conductivity for the fast gas diffusion and electron transfer, respectively. As shown in Fig. 1.5, the highly porous and nano-structured catalyst layers are fabricated to maximize the reaction surface area (tri-phase

boundary) where catalytically active particles, electrolyte phase, and gas pores intersect [1, 3].

In PEMFC operation, the cell potential (E) is decreased by the overpotential in the anode, cathode, and electrolyte. Therefore, E can be expressed by the following equation:

$$E = E_0 - \eta_{act,a} - \eta_{act,c} - \eta_{ohm} - \eta_{mt,a} - \eta_{mt,c} \quad (1\text{-}1)$$

Where, E_0 is the thermodynamic reversible potential, $\eta_{act,a}$ and $\eta_{act,c}$ are the activation overpotentials related to the charge transfer in the anode and cathode, respectively. η_{ohm} is the ohmic overpotential in the cell. $\eta_{mt,a}$ and $\eta_{mt,c}$ are the mass transfer overpotentials in the anode and cathode, respectively. Among the all overpotentials in PEMFC, it has been known that $\eta_{act,c}$ by the slow ORR and $\eta_{mt,c}$ by water flooding in the cathode are the main reasons for potential losses during the PEMFC operation. In Fig. 1.6, the polarization curve of PEMFC shows two large potential losses in the low and high potential regions, which are induced due to the charge transfer resistance of the ORR and mass transfer resistance of O_2, respectively [2].

Anode	$H_2\,(g) \longrightarrow 2H^+\,(aq) + 2e^-$	(E = 0.000 V)
Cathode	$\frac{1}{2}O_2\,(g) + 2H^+\,(aq) + 2e^- \longrightarrow H_2O\,(l)$	(E = 1.229 V)
Overall	$H_2\,(g) + \frac{1}{2}O_2\,(g) \longrightarrow H_2O\,(l)$	(E = 1.229 V)

Fig. 1.2 Anode and cathode reactions in PEMFC.

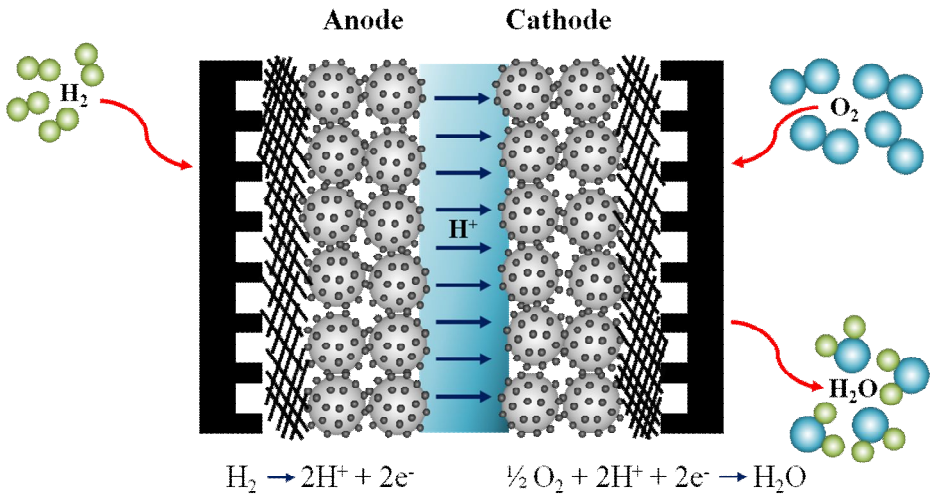

Fig. 1.3 Principle of PEMFC operation.

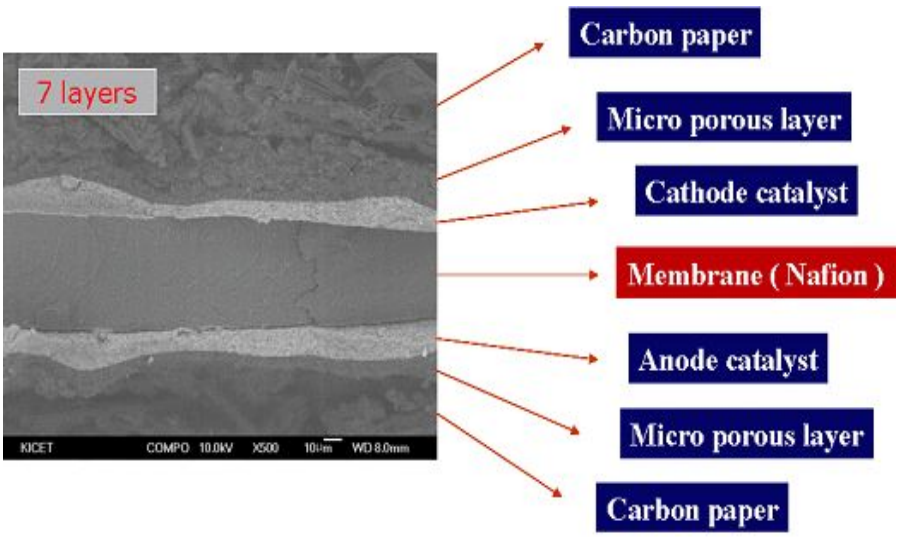

Fig. 1.4 Components of membrane electrode assembly (MEA).

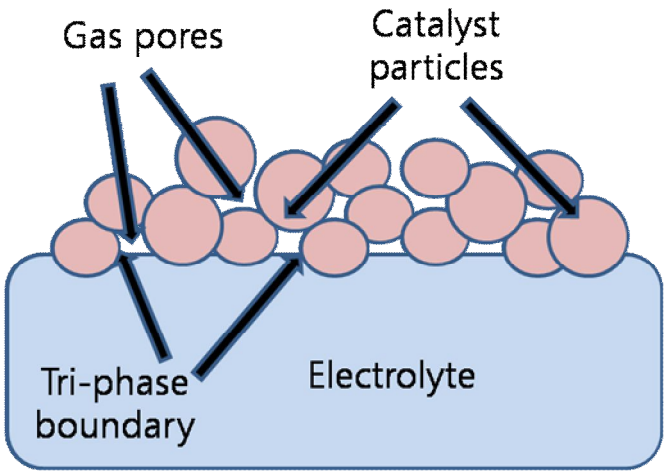

Fig. 1.5 Schematic diagram of tri-phase boundary in fuel cell.

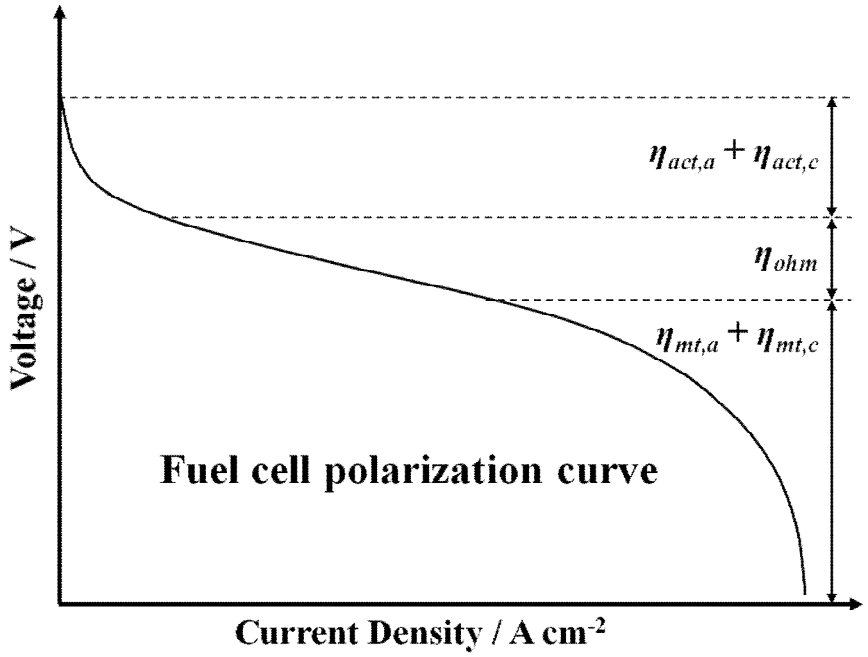

Fig. 1.6 Potential losses in fuel cell polarization curve.

1.2. Development of fuel cell catalysts

1.2.1. Fuel cell catalysts

Catalyst is the core material in fuel cell because the electrochemical reactions are occurred on the catalyst surface. It is composed of metal nanoparticle and support material as shown in Fig. 1.7. For the several decades, they have been developed to enhance the catalytic activity and active surface area. In the studies for high catalytic activity, various researches have been performed about particle size effect, ligand and strain effect by alloying, core-shell structure, shape control of nanoparticle, and so on [4-15]. Especially, to understand the basic characteristics of catalysts, the fundamental studies have been intensively conducted by utilization of the metal slabs with low index facets such as (111), (100), and (110) [16-21]. These efforts facilitated the application of highly active catalysts to PEMFC by reduction of overpotential of the ORR.

On the other hand, the support materials have been fabricated mainly to increase the surface area of the catalyst by uniformly loading metal nanoparticles on the support. Lots of carbon materials have been developed for the support material since they had high electron conductivity and many nano and micro pores [22-28]. In addition, nanoparticles could be easily loaded on the carbon support through the simple carbon surface modification such as an acid treatment. Highly distributed fuel cell catalyst using carbon supports such as vulcan, black pearl, carbon nanotube (CNT), carbon naofiber

(CNF), and various meso-porous carbons were applied to the fuel cell fabrication. Using the carbon support became a break-through in the development of fuel cell catalysts. Metal oxides as a support material have been also studied to maximize the strong metal-support interaction (SMSI) and to improve the catalytic activity [29, 30]. However, despite the SMSI, loading metal nanoparticles on metal oxide was very difficult.

Therefore, metal nanoparticle and support material of catalysts are the most important things for the fuel cell application. As mentioned in the section 1.1.2, the problems of the large charge transfer resistance of the ORR and mass transfer resistance of O_2 can be solved by reasonable design of nanoparticle and support material.

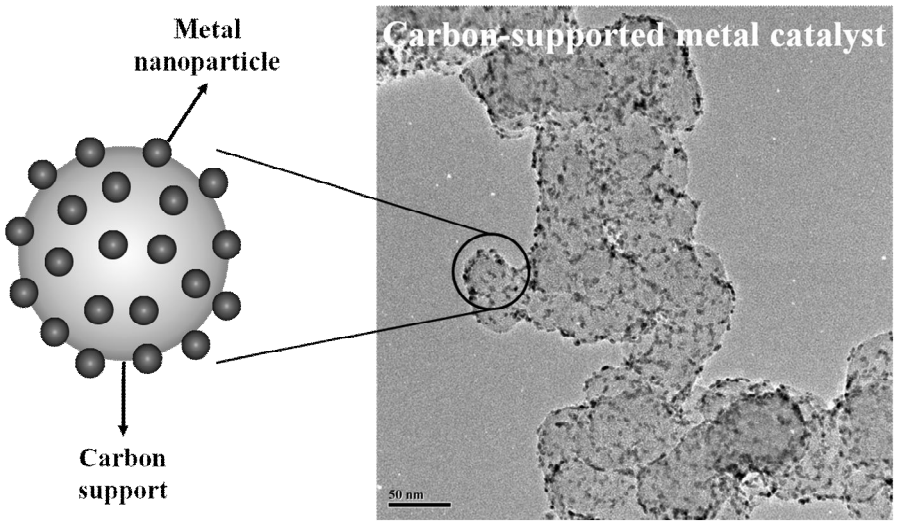

Fig. 1.7 Components of PEMFC catalyst.

1.2.2. Oxygen reduction reaction (ORR) in PEMFC cathode

In PEMFC, the cathode reaction is the ORR, in which molecular oxygen adsorbs to the catalyst surface and is reduced to water through four-electron pathway [31]. However, the ORR involving four electrons is more complex than the HOR due to the strong O-O bond, the formation of highly stable Pt-O or Pt-OH species, and the hydrogen peroxide (H_2O_2) generation.

In the PEMFC operation, the open circuit voltage (OCV) is lower than the theoretical reversible voltage (1.229 V), which is induced by extremely low cathodic exchange current density (i_0). The overall ORR in an acid electrolyte is shown as follows:

$$O_2 + 4H^+ + 4\ e^- \rightarrow 2H_2O \qquad (E_0)_{298K} = 1.229\ V \qquad (1\text{-}2)$$

The ORR is irreversible reaction even on Pt surface since it is conducted at high potential region under severe corrosive environment. It is known that various intermediates such as O, OH, and OOH adsorb on Pt surface in the ORR, which means that the mixed potential is occurred by the anodic current generation through the surface oxide formation (Pt-O and Pt-OOH). High surface coverage of adsorbed OH results in a decrease in the active sites for the O_2 adsorption and following reduction to water.

It is well known that the OH adsorption on Pt surface can be decreased by fabrication of PtM (M = Fe, Co, Ni) alloy catalysts [32-39]. Pt has intrinsically high binding energy between Pt surface and oxygen of the

oxygenated species such as O_2, O, OH, and OOH because *d*-band center of surface Pt is upward to the Fermi-level compared to that of the PtM alloy catalyst. As shown in Fig. 1.8, when PtM alloy is formed, the electron transfer is occurred from the transition metal such as Fe, Co, and Ni to Pt, which results in the band width broadening and downshift of Pt *d*-band center relative to the Fermi-level [35, 40]. It can be confirmed by measuring Pt 4f core level (CL) shift through the X-ray photoelectron spectroscopy (XPS). The downshift of Pt 4f CL induces the downshift of *d*-band center of Pt in the same direction in PtM alloy.

Recently, "Pt-skeleton" and "Pt-skin" structure fabricated from PtM alloy catalyst has been studied to improve the ORR activity more [41-43]. For instance, "Pt-skeleton" structure was formed by leaching out Ni on PtNi alloy surface through the chemical acid treatment, and "Pt-skin" structure was made by annealing the surface Pt of "Pt-skeleton" structure through the heat treatment [41]. The PtNi catalyst with "Pt-skin" structure showed much higher ORR activity than that with "Pt-skeleton" structure. It was attributed to preferential formation of highly active (111) surface and less NiO phase on "Pt-skin" structure compared to "Pt-skeleton" structure. However, the contribution between ligand and strain effects by Ni sublayer under Pt overlayers was not clearly distinguished. The ligand effects have been well known by the experimental results related to the transition metal alloying. The difference of electronegativity between Pt and the second metal solute causes the charge transfer, which results in the Pt electronic structure changes [44]. However, the surface strain effect was only calculated from the estimation of

lattice parameter difference between Pt overlayer and Ni sublayer. The surface strain effects are needed to be intensively studied to distinguish an exact contribution of the strain effects from that of the ligand effects.

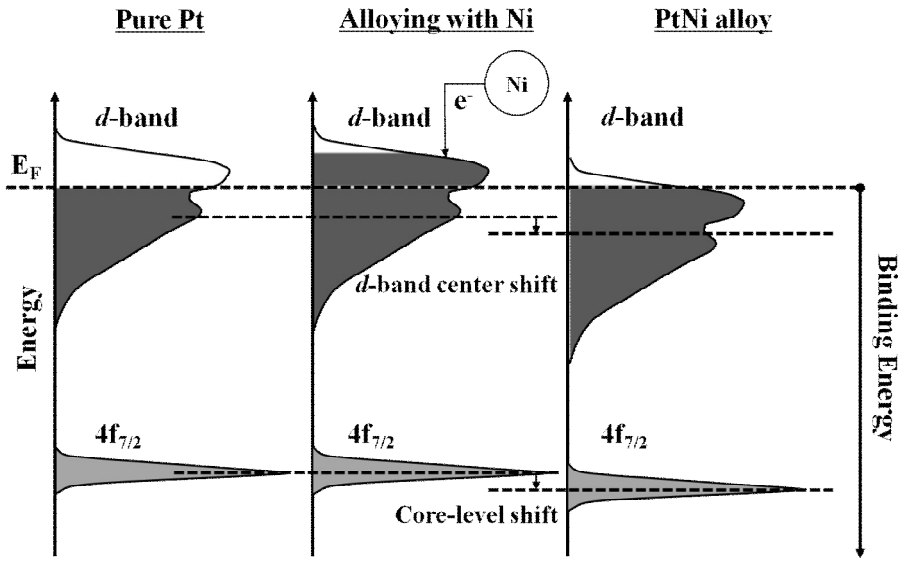

Fig. 1.8 *d*-band center and 4f core-level downshift by PtNi alloying.

1.2.3. Water management in PEMFC cathode

The water management in the MEA is one of the most important factors as well as the sluggish ORR since PEMFC always involves the production and transport of water in the MEA. As shown in Fig. 1.9, especially, the tri-phase boundary can be blocked by water produced by the ORR in the cathode, thereby resulting in water flooding [45, 46]. If water is not well removed from the catalyst layer, it severely inhibits the oxygen transport to catalyst surfaces in the cathode catalyst layer. In the polarization curve of PEMFC, the mass transfer overpotential increases rapidly with the increase of current density, and consequently it becomes the main reason for voltage loss during the PEMFC operation [46].

In recent decades, many researchers have developed various technologies to reduce water flooding in the cathode catalyst layer [47-52]. The technologies can be mainly categorized into two typical methods. The first involved the introduction of hydrophobic polymer particles into the cathode catalyst layer [47-49]. For instance, polytetraflouroethylene (PTFE) particles were mixed with carbon-supported metal catalysts in the catalyst ink preparation, and the catalyst layer with PTFE particles was formed [49, 52], or inserted PTFE particles were dissolved and adhered to the catalyst surface through an additional hot press procedure during the MEA fabrication [47, 48]. The second was related to pore formers such as carbonate [50, 51]. In this procedure, large gas pores to improve the oxygen and water transport could be formed by removing the inserted pore forming agent into the cathode catalyst

layer.

Despite the potential of these methods, several issues are yet to be overcome. First, when hydrophobic polymers adhere to the catalyst surfaces by a hot press procedure, they may be randomly distributed onto the surface. As a result, the metal catalyst surface, where the electrochemical reaction occurs, may be blocked along with carbon supports, which results in a fatal decrease in the electrochemical active surface (EAS) of catalysts [49]. In addition, the insertion of hydrophobic polymer particles or a pore forming agent into the catalyst layer makes the catalyst layer thickness increase to a certain extent, and thus the oxygen transport may become harder when the same catalyst loading is used in the MEA [49, 50].

Meanwhile, the related studies have been rarely concentrated on a carbon support for the improvement of the water transport in the MEA. Most of fuel cell catalysts have the carbon support with high surface area to disperse metal nanoparticles on the carbon surfaces. The use of carbon support in fuel cell catalysts gave a break-through, which facilitated low noble metal loading. However, to load nanoparticles on the carbon surfaces, carbon support should have hydrophilic functional groups on the surfaces. Accordingly, the acid treatment of carbon support is necessary to the carbon-supported catalyst synthesis. However, it can result in the water accumulation due to hydrophilic carbon surface in the PEMFC operation. Therefore, it is required to study the fundamental water flooding induced by the carbon support. To address the above problems, a simple method for efficient water management in the catalyst layer of PEMFC is potentially of great benefit.

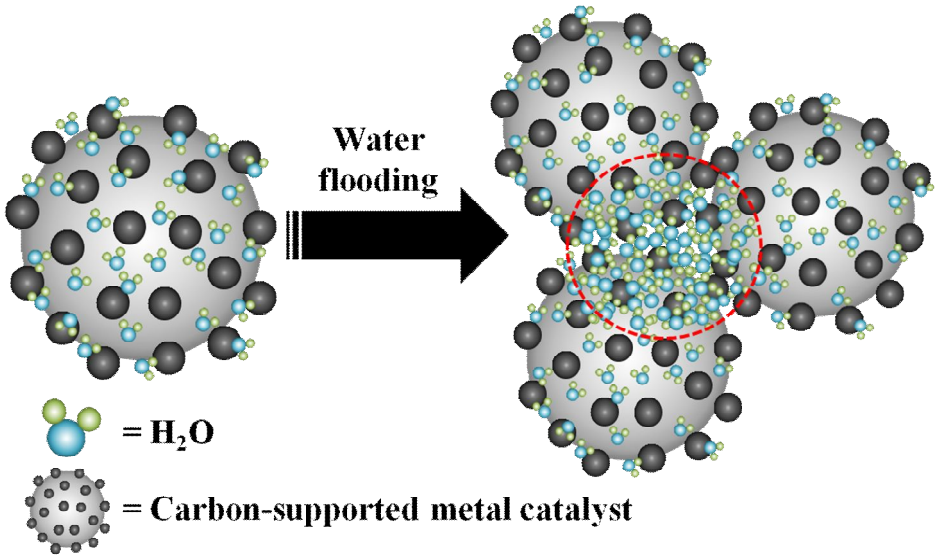

Fig. 1.9 Water flooding in carbon surface and catalyst agglomerates.

1.3. References

1. R.P. O'Hayre, S.-W. Cha, W. Colella, F.B. Prinz, FUEL CELL FUNDAMENTALS, John Wiley & Sons, New York, **2006**.

2. F. Barbir, PEM Fuel Cells: Theory and Practice, Elsevier Inc., London, **2005**.

3. A. Dhanda, H. Pitsch, R. O'Hayre, "Diffusion impedance element model for the triple phase boundary", *J. Electrochem. Soc.* **2011**, 158, B877.

4. U. A. Paulus, A. Wokaun, G. G. Scherer, T. J. Schmidt, V. Stamenkovic, V. Radmilovic, N. M. Markovic, P. N. Ross, "Oxygen reduction on carbon-supported Pt−Ni and Pt−Co alloy catalysts", *J. Phys. Chem. B* **2002**, 106, 4181.

5. K. J. J. Mayrhofer,* B. B Blizanac, M. Arenz, V. R. Stamenkovic, P. N. Ross, N. M. Markovic, "The Impact of geometric and surface electronic properties of Pt-catalysts on the particle size effect in electrocatalysis", *J. Phys. Chem. B* **2005**, 109, 14433.

6. I. E. L. Stephens, A. S. Bondarenko, U. Grønbjerg, J. Rossmeisl, I. Chorkendorff, "Understanding the electrocatalysis of oxygen reduction on platinum and its alloys", *Energy Environ. Sci.* **2012**, 5, 6744.

7. Hong Yang, "Platinum-based electrocatalysts with core–shell nanostructures", *Angew. Chem. Int. Ed.* **2011**, 50, 2674.

8. K. J.J. Mayrhofer, V. Juhart, K. Hartl, M. Hanzlik, M. Arenz, "Adsorbate-induced surface segregation for core–shell nanocatalysts",

Angew. Chem. Int. Ed. **2009**, 48, 3529.

9. T. K. Sau, A. L. Rogach, "Nonspherical noble metal nanoparticles: colloid-chemical synthesis and morphology control", *Adv. Mater.* **2010**, 22, 1781.

10. J. Wu, J. Zhang, Z. Peng, S. Yang, F. T. Wagner, H. Yang, "Truncated octahedral Pt_3Ni oxygen reduction reaction electrocatalysts", *J. AM. Chem. Soc.* **2010**, 132, 4984.

11. Y. Chen, Z. Liang, F. Yang, Y. Liu, S. Chen, "Ni–Pt core–shell nanoparticles as oxygen reduction electrocatalysts: effect of Pt shell coverage", *J. Phys. Chem. C* **2011**, 115, 24073.

12. J. R. Kitchin, J. K. Nørskov, M. A. Barteau, J.G. Chen, "Role of strain and ligand effects in the modification of the electronic and chemical properties of bimetallic surfaces", *Phys. Rev. Lett.* **2004**, 93, 156801.

13. M. P. Hyman, J. W. Medlin, "Effects of electronic structure modifications on the adsorption of oxygen reduction reaction intermediates on model Pt(111)-alloy surfaces", *J. Phys. Chem. C* **2007**, 111, 17052.

14. V. Stamenkovic, T. J. Schmidt, P. N. Ross, N. M. Markovic, "Surface segregation effects in electrocatalysis: kinetics of oxygen reduction reaction on polycrystalline Pt_3Ni alloy surfaces", *J. Anal. Chem.* **2003**, 554-555, 191.

15. C. Wang, H. Daimon, T. Onodera, T. Koda, S. Sun, "A general approach to the size- and shape-controlled synthesis of platinum nanoparticles and their catalytic reduction of oxygen", *Angew. Chem. Int.*

Ed. **2008**, 47, 3588.

16. V. Tripkovic, E. Skúlasona, S. Siahrostamia, J. K. Nørskov, J. Rossmeisl, "The oxygen reduction reaction mechanism on Pt(1 1 1) from density functional theory calculations", *Electrochim. Acta* **2010**, 55, 7975.

17. V. R. Stamenkovic, B. Fowler, B. S. Mun, G. Wang, P. N. Ross, C. A. Lucas, N. M. Markovic, "Improved oxygen reduction activity on Pt3Ni(111) via increased surface site availability", *Science* **2007**, 315, 493.

18. J. X. Wang, N. M. Markovic, R. R. Adzic, "Kinetic analysis of oxygen reduction on Pt(111) in acid solutions: intrinsic kinetic parameters and anion adsorption effects", *J. Phys. Chem. B* **2004**, 108, 4127.

19. V. Stamenkovic, N. M. Markovic, P.N. Ross Jr., "Structure-relationships in electrocatalysis: oxygen reduction and hydrogen oxidation reactions on Pt(111) and Pt(100) in solutions containing chloride ions", *J. Anal. Chem.* **2001**, 500, 44.

20. N. Markovic, H. Gasteiger, P. N. Ross, "Kinetics of oxygen reduction on Pt(hkl) electrodes: implications for the crystallite size effect with supported Pt electrocatalysts", *J. Electrochem. Soc.* **1997**, 144, 1591.

21. D. S. Strmcnik, P. Rebec, M. Gaberscek, D. Tripkovic, V. Stamenkovic, C. Lucas, N. M. Markovic, "Relationship between the surface coverage of spectator species and the rate of electrocatalytic reactions", *J. Phys. Chem. C* **2007**, 111, 18672.

22. F. Sua, C. K. Pohb, J. Zengc, Z. Zhongb, Z. Liud, J. Lin, "Pt nanoparticles supported on mesoporous carbon nanocomposites

incorporated with Ni or Co nanoparticles for fuel cells", *J. Power Sources* **2012**, 205, 136.

23. D. Banham, F. Feng, T. Fürstenhaupt, S. Ye,V. Birss, "First time investigation of Pt nanocatalysts deposited inside carbon mesopores of controlled length and diameter", *J. Mater. Chem.* **2012**, 22, 7164.

24. X. Bo, L. Zhu, G. Wang, L. Guo, "Template-free synthesis of rectangular mesoporous carbon nanorods and their application as a support for Pt electrocatalysts", *J. Mater. Chem.* **2012**, 22, 5758.

25.W. Yang, X. Wang, F. Yang, C. Yang, X. Yang, "Carbon nanotubes decorated with Pt nanocubes by a noncovalent functionalization method and their role in oxygen reduction", *Adv. Mater.* **2008**, 20, 2579.

26. H.-S. Oh, H. Kim, "Efficient synthesis of Pt nanoparticles supported on hydrophobic graphitized carbon nanofibers for electrocatalysts using noncovalent functionalization", *Adv. Funct. Mater.* **2011**, 21, 3954.

27. B. Wu, D. Hu, Y. Kuang, B. Liu, X. Zhang, J. Chen, "Functionalization of carbon nanotubes by an ionic-liquid polymer: dispersion of Pt and PtRu nanoparticles on carbon nanotubes and their electrocatalytic oxidation of methanol", *Angew. Chem. Int. Ed.* **2009**, 48, 4751.

28. D. Xiang, L. Yin, "Well-dispersed and size-tuned bimetallic PtFex nanoparticle catalysts supported on ordered mesoporous carbon for enhanced electrocatalytic activity in direct methanol fuel cells", *J. Mater. Chem.* **2012**, 22, 9584.

29. V. T. T. Ho, C.-J. Pan, J. Rick, W.-N. Su, B.-J. Hwang,

"Nanostructured $Ti_{0.7}Mo_{0.3}O_2$ support enhances electron transfer to Pt: high-performance catalyst for oxygen reduction reaction", *J. Am. Chem. Soc.* **2011**, 133, 11716.

30. S. H. Kang, T.-Y. Jeon, H.-S. Kim, Y.-E. Sung, W. H. Smyrl, "Effect of annealing PtNi nanophases on extended TiO_2 nanotubes for the electrochemical oxygen reduction reaction", *J. Electrochem. Soc.* **2008**, 155, B1058.

31. J. K. Nørskov, J. Rossmeisl, A. Logadottir, L. Lindqvist, J. R. Kitchin, T. Bligaard, H. Jonsson, "Origin of the overpotential for oxygen reduction at a fuel-cell cathode", *J. Phys. Chem. B* **2004**, 108, 17886.

32. V. Mazumder, M. Chi, K. L. More, S. Sun, "Core/shell Pd/FePt nanoparticles as an active and durable catalyst for the oxygen reduction reaction", *J. Am. Chem. Soc.* **2010**, 132, 7848.

33. U. A. Paulus, A. Wokaun, G. G. Scherer, T. J. Schmidt, V. Stamenkovic, N. M. Markovic, P. N. Ross, "Oxygen reduction on high surface area Pt-based alloy catalysts in comparison to well defined smooth bulk alloy electrodes", *Electrochim. Acta* **2002**, 47, 3787.

34. T.-Y. Jeon, S. J. Yoo, Y.-H. Cho, K.-S. Lee, S. H. Kang, Y.-E. Sung, "Influence of oxide on the oxygen reduction reaction of carbon-supported Pt−Ni alloy nanoparticles", *J. Phys. Chem. C* **2009**, 113, 19732.

35. T. Toda, H. Igarashi, H. Uchida, M. Watanabe, "Enhancement of the electroreduction of oxygen on Pt alloys with Fe, Ni, and Co", *J. Electrochem. Soc.* **1999**, 146, 3750.

36. J. R. C. Salgado, E. Antolini, E. R. Gonzalez, "Structure and activity

of carbon-supported Pt−Co electrocatalysts for oxygen reduction", *J. Phys. Chem. B* **2004**, 108, 17767.

37. J. Kim, Y. Lee, S. Sun, "Structurally ordered FePt nanoparticles and their enhanced catalysis for oxygen reduction reaction", *J. Am. Chem. Soc.* **2010**, 132, 4996.

38. Y. Liu, C. M. Hangarter, U. Bertocci, T. P. Moffat, "Oxygen reduction reaction on electrodeposited $Pt_{100-x}Ni_x$: influence of alloy composition and dealloying", *J. Phys. Chem. C* **2012**, 116, 7848.

39. T.-Y. Jeon, S. J. Yoo, Y.-H. Cho, S. H. Kang, Y.-E. Sung, "Effect of de-alloying of Pt–Ni bimetallic nanoparticles on the oxygen reduction reaction", *Electrochem. Commun.* **2010**, 12, 1796.

40. M. Wakisaka, S. Mitsui, Y. Hirose, K. Kawashima, H. Uchida, M. Watanabe, "Electronic structures of Pt−Co and Pt−Ru alloys for CO-tolerant anode catalysts in polymer electrolyte fuel cells studied by EC−XPS", *J. Phys. Chem. B* **2006**, 110, 23489.

41. C. Wang, M. Chi, D. Li, D. Strmcnik, D. Vliet, G. Wang, V. Komanicky, K.-C. Chang, A. P. Paulikas, D. Tripkovic, J. Pearson, K. L. More, N. M. Markovic, V. R. Stamenkovic, "Design and synthesis of bimetallic electrocatalyst with multilayered Pt-skin surfaces", *J. Am. Chem. Soc.* **2011**, 133, 14396.

42. S. Chen, W. Sheng, N. Yabuuchi, P. J. Ferreira, L. F. Allard, Y. Shao-Horn, "Origin of oxygen reduction reaction activity on "Pt_3Co" nanoparticles: atomically resolved chemical compositions and structures", *J. Phys. Chem. C* **2009**, 113, 1109.

43. D. F. Vliet, C. Wang, D. Li, A. P. Paulikas, J. Greeley, R. B. Rankin, D. Strmcnik, D. Tripkovic, N. M. Markovic, V. R. Stamenkovic, "Unique electrochemical adsorption properties of Pt-Skin surfaces", *Angew. Chem. Int. Ed.* **2012**, 51, 3139.

44. K.-W. Park, J.-H. Choi, B.-K. Kwon, S.-Ah Lee, Y.-E. Sung, H.-Y. Ha, S.-A. Hong, H. Kim, A. Wieckowski, "Chemical and electronic effects of Ni in Pt/Ni and Pt/Ru/Ni alloy nanoparticles in methanol electrooxidation", *J. Phys. Chem. B* **2002**, 106, 1869.

45. H. Li, Y. Tang, Z. Wang, Z. Shi, S. Wu, D. Song, J. Zhang, K. Fatih, J. Zhang, H. Wang, Z. Liu, R. Abouatallah, A. Mazza, "A review of water flooding issues in the proton exchange membrane fuel cell", *J. Power Sources* **2008**, 178, 103.

46. P. P. Mukherjee, Q. Kang, C.-Y. Wang, "Pore-scale modeling of two-phase transport in polymer electrolyte fuel cells—progress and perspective", *Energy Environ. Sci.* **2011**,4, 346.

47. X. Zhang, P. Shi, "Dual-bonded catalyst layer structure cathode for PEMFC", *Electrochem. Commun.* **2006**, 8, 1229.

48. M. Uchida, Y. Aoyama, N. Eda, A. Ohta, "Investigation of the microstructure in the catalyst layer and effects of both perfluorosulfonate ionomer and PTFE-loaded carbon on the catalyst layer of polymer electrolyte fuel cells", *J. Electrochem. Soc.* **1995**, 142, 4143.

49. R. Friedmann, T. V. Nguyen, "Optimization of the microstructure of the cathode catalyst layer of a PEMFC for two-phase flow", *J. Electrochem. Soc.* **2010**, 157, B260.

50. J. Zhao, X. Hea, L. Wang, J. Tian, C. Wan, C. Jiang, "Addition of NH4HCO3 as pore-former in membrane electrode assembly for PEMFC", *Int. J. Hydrogen Energ.* **2007**, 32, 380.

51. T. V. Reshetenko, H.-T. Kim, H.-J. Kweon, "Cathode structure optimization for air-breathing DMFC by application of pore-forming agents", *J. Power Sources* **2007**, 171, 433.

52. N. Jung, Y.-H. Cho, M. Ahn, J. W. Lim, Y. S. Kang, D. Y. Chung, J. Kim, Y.-H. Cho, Y.-E. Sung, "Methanol-tolerant cathode electrode structure composed of heterogeneous composites to overcome methanol crossover effects for direct methanol fuel cell", *Int. J. Hydrogen Energ.* **2011**, 36, 15731.

Chapter 2. Experimental

2.1. Surface modification of PtNi alloy catalyst

2.1.1. Preparation of carbon-supported PtNi alloy catalyst

Carbon-supported PtNi (PtNi/C) alloy nanoparticles were prepared via conventional sodium borohydride ($NaBH_4$) reduction in anhydrous ethanol [1]. 0.15 g of carbon black (Vulcan XC-72R) was dispersed in anhydrous ethanol (150 mL), and the mixture solution was stirred at 500 rpm for 1 h, followed by sonication for 1 hr. $PtCl_4$ (0.0853 g), $NiCl_2 \cdot 6H_2O$ (0.0602 g), and sodium acetate (0.9143 g) were added to the ethanol solution containing dispersed carbon black. Stirring for 2 hr and sonication for 10 min of the solution were repeated two times. The amount of sodium acetate added to the mixture was adjusted so that the molar ratio of sodium acetate to total metal was 22. After stirring and sonication of the solution, 20 mL of anhydrous ethanol solution with $NaBH_4$ was quickly introduced with vigorous stirring (750 rpm). The resultant solution was stirred for 4 h to complete the reduction of metal precursors, followed by filtration, washing, and drying in an oven at 60 °C. As-prepared PtNi/C by above synthetic method is referred to as PtNi/C-ASP in this thesis.

2.1.2. Surface structure modifications of PtNi alloy catalyst

To leach out the surface Ni on PtNi/C-ASP, PtNi/C-ASP was stirred at 500 rpm for 2.5 hr in 0.5 M $HClO_4$ solution (500 mL). After the acid treatment, the solution was washed by filtration with excessive D.I. water, and dried in an oven at 60 °C. This acid-treated PtNi/C is referred to as PtNi/C-acid. In addition, PtNi/C-acid was heated at 250 °C for 30 min in H_2 atmosphere to smoothen the surface of PtNi/C-acid which might have corrugated surface structure. This heat-treated PtNi/C-acid is referred to as PtNi/C-acid/heat.

Ultimately, to understand the effects of surface structure of core materials on Pt overlayer, Pt overlayers were additionally deposited on PtNi/C-acid and PtNi/C-acid/heat, respectively. They are referred to as Pt@PtNi/C-acid and Pt@PtNi/C-acid/heat, respectively. L-ascorbic acid (0.15 g) was dispersed in anhydrous ethanol (200 mL) for 10 min by sonication. PtNi/C-acid (0.09 g) or PtNi/C-acid/heat (0.09 g) was introduced in the solution, and mixed by sonication for 10 min and stirring for 1 hr [2]. After $PtCl_4$ (0.0173 g) as a precursor of Pt overlayer was dispersed in the solution, the solution was refluxed and stirred at 80 °C for 2 hr. The solution was then washed by filtration with excessive D.I. water, and dried in an oven at 60 °C. 7 wt.% of Pt@PtNi/C-acid and Pt@PtNi/C-acid/heat were the numerical weight of additional Pt overlayer, respectively.

2.2. Surface modification of carbon support

2.2.1. Selective functionalization of carbon-supported Pt catalyst

40 wt.% carbon-supported Pt (Pt/C) (Johnson Matthey) was dispersed with amine-terminated poly(N-isopropylacrylamide) (PNIPAM) (Aldrich) of 0.04 mmol in a solvent of pH 1.6, which composed of isopropyl alcohol (IPA) (Aldrich) and $HClO_4$ (Aldrich). After the solution was well mixed for 1 hr, 1-ethyl-3-(3-dimethylaminopropyl)carbodiimide (EDC) (Fluka) of 0.04 mmol as a catalyst was quickly introduced into the vigorously stirred solution for the amide reaction between -COOH of the carbon surface and $-NH_2$ of amine-terminated PNIPAM [3]. The solution was washed through the filtration by excessive D.I. water after the amide reaction finished by EDC for 3 hr. Finally, the filtered catalyst powder was dried at 60 °C. The carbon surface-modified Pt/C by PNIPAM is referred to as Pt/C-PNIPAM in this thesis.

2.2.2. Membrane electrode assembly (MEA) fabrication

The MEAs were prepared with and without PNIPAM in the cathode. A catalyst ink for the cathode catalyst layer with PNIPAM was fabricated by mixing Pt/C-PNIPAM, 5 wt.% Nafion ionomer solution (Aldrich) and IPA. Non-treated 40 wt.% Pt/C was used in an anode catalyst ink instead

of Pt/C-PNIPAM. In the MEA without PNIPAM, the anode and cathode catalyst inks identically had non-treated 40 wt.% Pt/C. The prepared catalyst inks were sprayed onto the anode and cathode parts of the Nafion 212 membrane (Dupont). Nafion 212 membrane was used after the pretreatment in which the membranes were boiled in 3 % hydrogen peroxide solution, 0.5 M H_2SO_4, and D.I. water at 80 °C in order [4]. The Pt loadings were equally 0.2 mg cm^{-2} in the cathodes and anodes of the MEAs, respectively. The catalyst-coated membranes (CCMs) were sandwiched between the anode and cathode GDLs (SGL 35 BC) without hot press process as shown in Fig. 2.1.

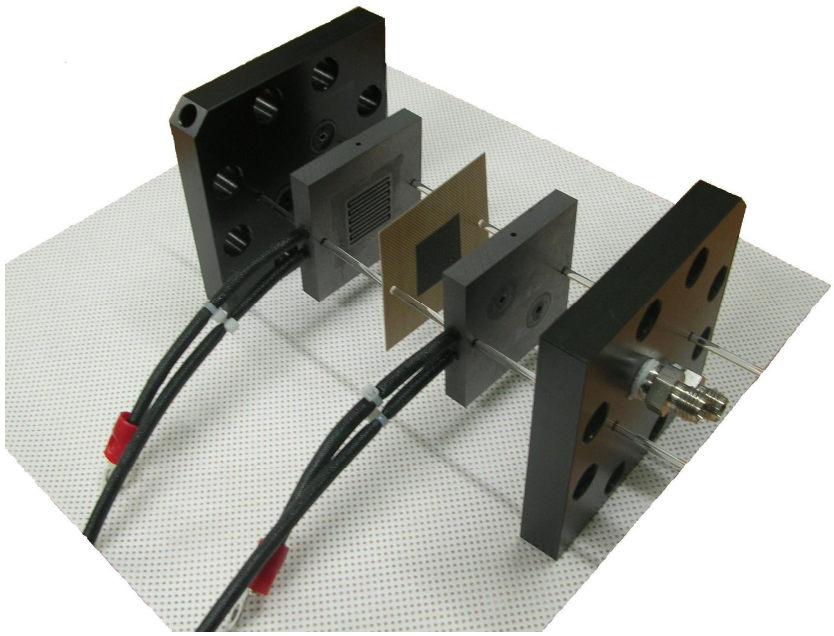

Fig. 2.1 Components of unit cell.

2.3. Electrochemical characterization

In the experiment related to the surface modifications of PtNi alloy catalysts, all electrochemical measurements were conducted in a standard three-compartment electrochemical cell using a glassy carbon electrode of the rotating disk electrode (RDE), Pt wire, and saturated calomel electrode (SCE) as working, counter, and reference electrodes, respectively. All measurements were recorded and reported versus reversible hydrogen electrode (RHE), and performed at 20 °C in 0.1 M $HClO_4$. The catalyst ink slurry was prepared by mixing PtNi/C catalysts with 20 μL of DI water, 54.7 μL of 5 wt % Nafion solution as a binding material, and 630 μL of 2-propanol. Following mixing and ultrasonication, a drop of ink slurry was loaded onto a glassy carbon substrate (0.196 cm^2, geometric surface area). The dried electrode was then transferred to the electrochemical cell.

In the CO stripping current measurement, CO was adsorbed on prepared PtNi/C catalysts at 0.05 V during the introduction of 100 % CO gas for 20 min [5]. The electrolyte was purged by Ar gas for 25 min after CO_{ad} adsorbed on the catalyst surfaces, and CO_{ad} was then oxidized by the potential sweep between 0.05 and 1.05 V with a scan rate of 20 mV s^{-1}. Cyclic voltammogram was obtained by the potential sweep method between 0.05 and 1.05 V with a scan rate of 20 mV s^{-1} after purging the electrolyte by Ar gas for 20 min. The N_2O reduction current was measured to identify the potential of zero total charge (PZTC) [6]. After

N_2O gas was supplied into the electrolyte for 20 min, N_2O was reduced by scanning the potential between 0.05 and 0.7 V with a scan rate of 20 mV s^{-1} in continuously purging N_2O gas. The rotating speed of RDE was 1600 rpm in the N_2O reduction. The ORR test was conducted to confirm the ORR activity of prepared samples. Before the ORR test, a blank CV was measured with rotating speed of 1600 rpm by 5 mV s^{-1} in the potential between 0.05 and 1.05 V. After O_2 gas was purged for 30 min, the potential was scanned with rotating speed of 1600 rpm by 5 mV s^{-1} from 0.05 to 1.05 V with purging O_2 gas. The ORR curve was corrected by the anodic current of the blank CV.

In the experiment about the surface modification of carbon support by PNIPAM, all the electrochemical characterizations were performed with the MEAs in the unit cells. The CV was obtained at 100 mV s^{-1} between 0.05 and 1.0 V to compare the electrochemical active surfaces (EAS) of the prepared cathode catalyst layers [7]. Humidified H_2 and N_2 were supplied to the anode and cathode, respectively. For the unit cell performance test, humidified H_2 (150 ml min^{-1}) and air (800 ml min^{-1}) were flowed into the anode and cathode, respectively, at 70 °C. Electrochemical impedance spectroscopy (EIS) (IM6, Zahner) of the unit cells was measured at 0.65 V with an amplitude of 10 mV. The measurement was conducted in a frequency range from 0.1 Hz to 10 kHz. The ZView program (Scribner Associates, Inc.) was utilized to fit the EIS data, and a simple equivalent circuit was applied as shown in Fig. 2.2.

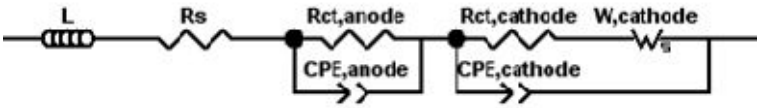

Fig. 2.2 Equivalent circuit of PEMFC. (L: inductance of wire, R_s: series resistance, R_{ct}: charge transfer resistance, CPE: constant phase element, W: Warburg impedance)

2.4. Physical and electronic structure measurements

The particle distribution and size of the surface modified PtNi/C catalysts were investigated by high resolution-transmission electron microscope (HR-TEM) (JEOL 2010, at 200 kV). The element analyzer (EA) (EA1112, CE Instrument) was used to identify the weight percent of surface modified PtNi/C catalysts. Total metal loading was calculated by subtracting the weight of C, H, N in a sample. Inductively coupled plasma-atomic emission spectroscopy (ICP-AES) (Optima-4300 DV, Perkin-Elmer) was performed to the compositions of prepared PtNi/C catalysts. By X-ray diffraction (XRD) (Rigaku, D/MAX 2500) with Cu Kα radiation (40 kV, 200 mA), the diffraction patterns of PtNi/C catalysts were obtained in 2 theta ranges between 20 and 80 °.

Pt L_{III} edge and Ni K edge X-ray absorption spectroscopy (XAS) was recorded at the Pohang Light Source (PLS) using the 10C beamline with a ring current of 120-170 mA at 2.5 GeV (Fig. 2.3). A Si(111) monochromator crystal was used with intensity detuned to 85% to eliminate high-order harmonics. Data were collected in fluorescence and transmission modes. Energy calibrations were performed for all measurements using either Pt foil or Ni foil placed in front of the third ion chamber. The University Washington data analysis program was the data analysis package used for X-ray absorption near-edge structure spectroscopy (XANES). The XANES spectra were first subjected to background removal by fitting pre-edge data to a Victoreen-type formula

over a range of 200-40 eV below the edge, followed by extrapolation over the energy range of interest and subtraction from the data. After removal of all background, second derivatives calculated from inflection points of data from the reference channel were used to correct the spectra for edge-shifts. Normalization was performed by the conventional procedures. The normalization value was chosen as the absorbance at the inflection point of one extended X-ray absorption fine structure (EXAFS) oscillation. The spectra were thus normalized by dividing each datum point by the normalization value.

In the experiment of the surface modification of carbon support, field emission-scanning electron microscopy (FE-SEM) was conducted using a SUPRA 55VP (Carl Zeiss) to measure the thickness and structure of the cathode catalyst layers with and without PNIPAM. The cross-section of the samples was obtained by breaking them in a second or less after putting them into liquid nitrogen for several minutes. Atomic force microscopy (AFM) was carried out to identify the surface structure and roughness of Pt/C catalysts. X-ray photoelectron spectra (XPS) were obtained from an Al Kα source (ESCALAB 250 XPS spectrometer, VG Scientifics). Binding energies were calibrated with respect to C (1s) at 285 eV. Experimental data were curve-fitted using XPSPEAK4.1 software. Atomic ratios of Pt oxidation states were estimated from the area of the respective Lorentzian-Gaussian peaks. The advancing and receding contact angles were measured when a water droplet with total volume of about 20 μl was drawn in and out onto each cathode catalyst

layer with and without PNIPAM using a contact angle analyzer (KRUSS, DSA 100). It was conducted at 20 and 70 °C.

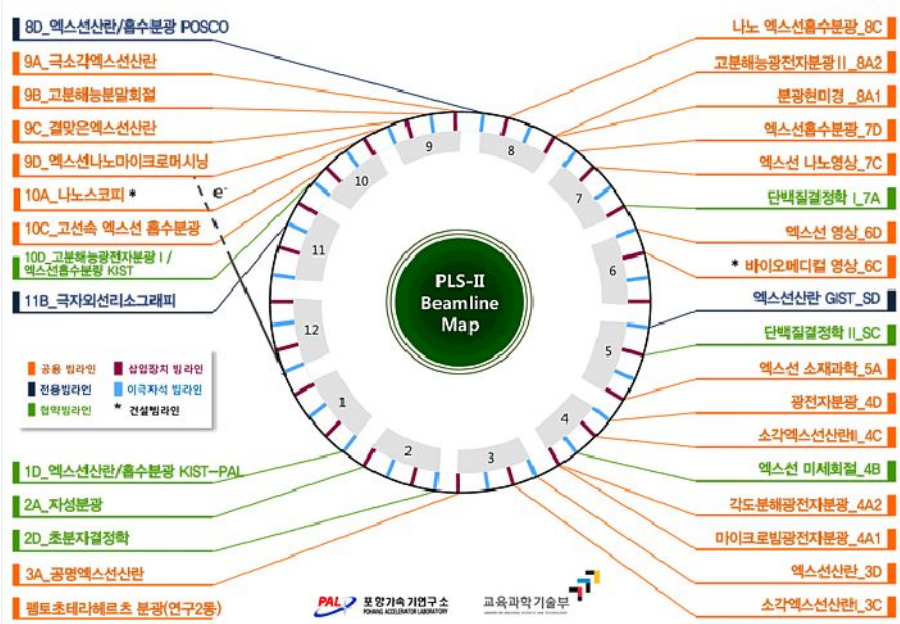

Fig. 2.3 Pohang light source (PLS) beam status. From the web page, http://pal.postech.ac.kr.

2.5. References

1. T.-Y. Jeon, S. J. Yoo, Y.-H. Cho, K.-S. Lee, S. H. Kang, Y.-E. Sung, "Influence of oxide on the oxygen reduction reaction of carbon-supported Pt?Ni alloy nanoparticles", *J. Phys. Chem. C* **2009**, 113, 19732.

2. K.-S. Lee, S. J. Yoo, D. Ahn, T.-Y. Jeon, K. H. Choi, I.-S. Park, Y.-E. Sung, "Surface structures and electrochemical activities of Pt overlayers on Ir nanoparticles", *Langmuir* **2011**, 27, 3128.

3. N. Nakajima, Y. Ikada, "Mechanism of amide formation by carbodiimide for bioconjugation in aqueous media", *Bioconjugate Chem.* **1995**, 6, 123.

4. Y.-H. Cho, H.-S. Park, Y.-H. Cho, D.-S. Jung, H.-Y. Park, Y.-E. Sung, "Effect of platinum amount in carbon supported platinum catalyst on performance of polymer electrolyte membrane fuel cell", *J. Power Sources* **2007**, 172, 89.

5. T.-Y. Jeon, S. J. Yoo, Y.-H. Cho, S. H. Kang, Y.-E. Sung, "Effect of de-alloying of Pt-Ni bimetallic nanoparticles on the oxygen reduction reaction", *Electrochem. Commun.* **2010**, 12, 1796.

6. K.-S. Lee, S. J. Yoo, D. Ahn, S.-K. Kim, S. J. Hwang, Y.-E. Sung, H.-J. Kim, E.A. Cho, D. Henkensmeier, T.-H. Lim, J. H. Jang, "Phosphate adsorption and its effect on oxygen reduction reaction for PtxCoy alloy and Aucore–Ptshell electrocatalysts", *Electrochim. Acta* **2011**, 56, 8802.

7. J. W. Lim, Y.-H. Cho, M. Ahn, D. Y. Chung, Y.-H. Cho, N. Jung, Y. S. Kang, O.-H. Kim, M. J. Lee, M. Kim, Y.-E. Sung, "Ionic resistance of a cathode catalyst layer with various thicknesses by electrochemical

impedance spectroscopy for PEMFC", *J. Electrochem. Soc.* **2012**, 159, B378.

Chapter 3. Results and Discussion

3.1. Effects of surface structure of core material on Pt overlayer

3.1.1. Effects of surface structure of de-alloyed PtNi catalysts

PtNi/C-ASP was synthesized by the impregnation method using $NaBH_4$ in anhydrous ethanol. To leach out Ni from the surface of PtNi/C-ASP, the acid treatment was then conducted on PtNi/C-ASP, and PtNi/C-acid with "Pt-skeleton"-like structure was fabricated. Continuously, PtNi/C-acid was heated at H_2 environment to make the "Pt-skin"-like structure. To analyze the metal composition and loading variation of the samples, ICP-AES and EA were performed, and the data were presented in Table 3.1. By the ICP-AES, it was confirmed that the atomic ratio of Pt to Ni ([Pt]/[Ni]) in PtNi/C-ASP and PtNi/C-acid were 1 and 3, respectively. It shows that the Ni was even much leached out from the surface on the PtNi/C-ASP rather than Pt. In addition, the metal loading in PtNi/C-acid was decreased by 3.6 wt.% by the acid treatment. The metal composition and loading of PtNi/C-acid/heat was not changed since PtNi/C-acid was only heated without any additional process.

As shown in Fig. 3.1, PtNi nanoparticles were properly dispersed on carbon supports regardless of post-treatments such as de-alloying by acid solution and following heating process. In addition, the particle sizes of

PtNi/C-ASP and PtNi/C-acid were hardly changed compared to PtNi/C-ASP when they were calculated by Scherrer equation in (220) peak of XRD in Table 3.1. It may be estimated that only surface atoms on PtNi/C-acid were leached out, and overall particle size of PtNi/C-acid was kept with Pt-rich surface structure. On the other hand, the particle size of PtNi/C-acid/heat was slightly increased by ~0.2 nm because the heat could make the Pt atoms diffused despite relatively low temperature (250 °C).

2 theta angles of PtNi/C-acid and PtNi/C-acid/heat were shifted toward lower than that of PtNi/C-ASP as shown in Fig. 3.2. It shows that Pt and Ni in PtNi alloy were de-alloyed when Ni atom was leached out by the acid treatment in PtNi/C-acid. However, both PtNi/C-acid and PtNi/C-acid/heat had still higher angles than pure Pt due to the effects of Ni in the core parts. Additionally, the XRD pattern of PtNi/C-acid/heat had sharper peaks compared to other samples, which indicates the increased crystallinity after annealing [1]. These observations, in addition to the absence of the peak separation of Pt and Ni phases, show that the bimetallic catalyst preserved the alloy properties after the applied treatment.

To intensively study the surface structure of the samples, the CO oxidation measurement was conducted in the acidic medium. As shown in Fig. 3.3, the CO oxidation peaks are typically distinguished by three peaks [2]. The pre-ignition peak at below 0.7 V is generated by defect sites on both (111) and (100) facets. The second peak between 0.7 and 0.8

V is related to (111) facet (former peak) and vicinal facet between (111) and (100) (latter peak). The single peak between 0.8 and 0.9 V is mainly attributed to (100) facet. As shown in Fig. 3.4a, PtNi/C-ASP showed only a broad CO stripping current peak between 0.7 and 0.9 V except the pre-ignition peak below 0.7 V. The high current density of the pre-ignition peak indicates lots of irregular defect sites such as surface step/edge and kink were on the surface of PtNi/C-ASP because the PtNi alloy might be much quickly formed by a strong reducing agent, $NaBH_4$. In addition, it was confirmed that the irregular surface structure did not have the long-range facets such as (111) and (100) since the main peak of CO stripping current was not separated into two typical peaks at above 0.7 V. The maximum CO oxidation peak potential was appeared at ~0.75 V in the potential region of a near-(111) facet. Since (111) facet had the most stable surface energy, it was made as the sample prepared, but it seemed not to have an ordered structure. However, after the acid treatment, the main peak of the CO stripping current started to split to the both directions of low and high potentials with 0.75 V as the center in PtNi/C-acid. Moreover, the pre-ignition peak of PtNi/C-acid was considerably reduced below 0.7 V. It is thought that the irregular defect atoms on (100) were firstly leached out, and near-(100) facet was appeared between 0.75 and 0.85 V after the acid treatment because the pre-ignition peak was affected especially by (100) facet rather than (111) facet [3, 4]. However, (111) facet was not clearly distinguished from (100) facet. Continuously, after the heat treatment, the CO oxidation current peak of PtNi/C-

acid/heat was more distinctly divided to two characteristic peaks of (111) and (100) by a decrease in the peak portion at 0.75 V related to the low coordination sites. These relatively ordered facets identified from the CO oxidation peaks correspond to the increase in crystallinity of PtNi/C-acid/heat in the XRD peaks. In addition, the potentials at the maximum peaks were confirmed by the first derivative curves of the CO oxidation currents in Fig. 3.4b. The maximum CO oxidation peak related to (111) facet of PtNi/C-acid/heat was more negatively shifted compared to that of PtNi/C-acid. It seemed that the surface structure of PtNi/C-acid was reconstructed after the heat treatment. It was expected that these structural modifications of PtNi/C samples affected the *d*-band center of Pt and binding energy between Pt and oxygenated species.

The electronic structures of Pt were investigated by the synchrotron XAS measurement. The XANES region of Pt L_{III} in the XAS can be used for assessing qualitative changes in the fractional *d*-band occupancies of Pt. It was thought that the coordination numbers of PtNi/C samples were not the same because different surface structures were confirmed from the CO stripping and XRD measurements. As shown in Fig. 3.5a, the white line absorption peaks of Pt L_{III} in PtNi/C samples were decreased in order; PtNi/C-ASP > PtNi/C-acid > PtNi/C-acid/heat. The reduction of the coordination numbers of PtNi/C-acid and PtNi/C-acid/heat was related to the surface modification through the surface de-alloying and reconstruction. As the lots of defect sites and surface oxides in PtNi/C-ASP were decreased after the acid treatment, PtNi/C-acid had higher

coordination number than PtNi/C-ASP despite the existence of partially low coordinated surface Pt atoms. For the same reason, the white line absorption of PtNi/C-acid was also decreased compared to that of PtNi/C-ASP in the XANES region of Ni K in Fig. 3.5b. PtNi/C-acid/heat could have more stable and ordered surface structure, which resulted in the lowest white line absorption peak at Pt L_{III} edge by smoothing the corrugated surface of PtNi/C-acid. On the other hand, in the XANES region of Ni K of PtNi/C-acid and PtNi/C-acid/heat, the order of the white line absorption peaks was reversed in Fig. 3.5b. It was attributed to an increase in Ni oxide and the electron transfer from Ni to Pt in the inner part of PtNi/C-acid/heat when the heat treatment was performed [5].

However, it was still ambiguous to explain the relation between the surface morphology and electronic structure changes since the X-ray transmitted not only the surface but also overall particles. Therefore, in order to identify the surface work functions of PtNi/C samples, the potential of zero charge (PZTC) was measured in an acidic medium. The high work function of a material is directly related to the high binding energy, and the high PZTC means high binding energy and downshift of *d*-band center of Pt relative to the Fermi-level [6, 7]. As shown in Fig. 3.6, PtNi/C-acid/heat showed the highest PZTC among prepared PtNi/C samples, and it is expected that the oxygenated species are weakly adsorbed on PtNi/C-acid/heat. Therefore, it was ensured that above results from XRD, CO oxidation current, and XANES corresponded to the PZTC data.

Based on above experimental results, CVs of PtNi/C-acid and PtNi/C-acid/heat were measured in 0.1 M $HClO_4$. As shown in Fig. 3.7, in the potential region of the Pt oxide formation, PtNi/C-acid/heat indicated lower Pt oxidation current than PtNi/C-acid. Additionally, in the cathodic sweep, the Pt reduction peak of PtNi/C-acid/heat was earlier appeared at higher potential [8]. It means that the binding energy between Pt and oxygenated species weakened in PtNi/C-acid/heat. Finally, as shown in Fig. 3.8, PtNi/C-acid/heat showed much higher ORR activity than PtNi/C-acid by the surface morphology and electronic structure changes.

Table 3.1 Physical properties of PtNi/C-ASP, PtNi/C-acid, and PtNi/C-acid/heat obtained from ICP-AES, EA, and XRD.

	PtNi/C-ASP	PtNi/C-acid	PtNi/C-acid/heat
Wt.%	33.6	30	30
Atomic Ratio (Pt : Ni)	1 : 1	3 : 1	3 : 1
Weight Ratio (Pt : Ni)	3.3 : 1	10 : 1	10 : 1
Particle Size (nm)	2.4	2.4	2.6
Lattice Parameter (nm)	0.3793	0.3798	0.3847

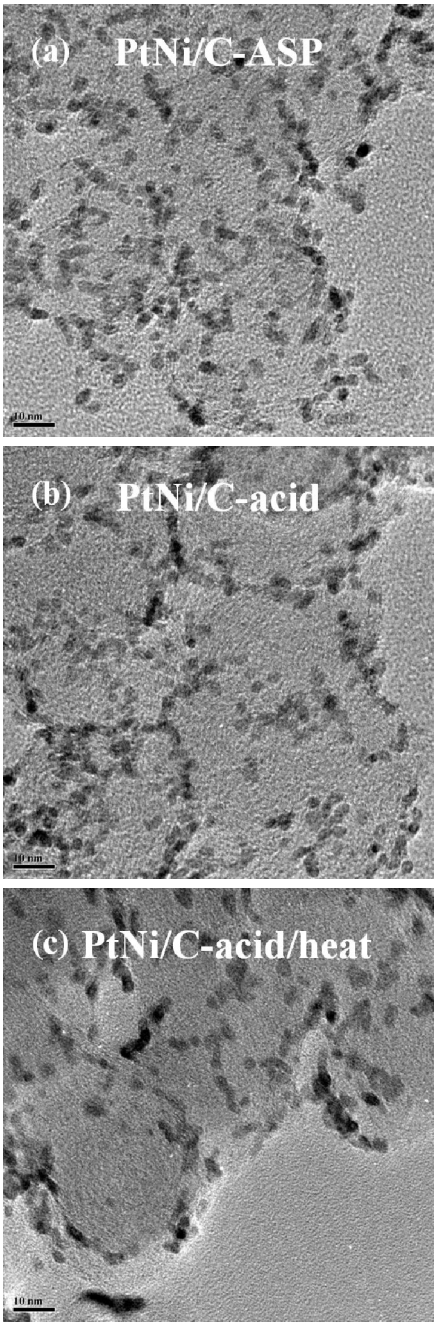

Fig. 3.1 TEM images of (a) PtNi/C-ASP, (b) PtNi/C-acid, and (c) PtNi/C-acid/heat.

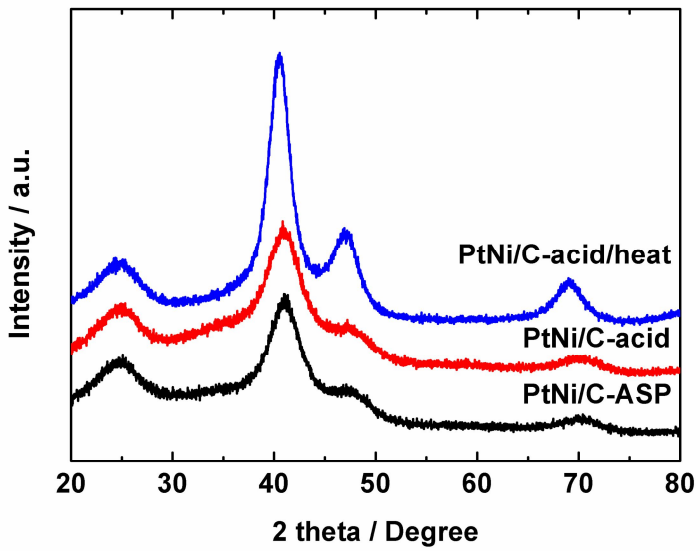

Fig. 3.2 XRD patterns of PtNi/C-ASP, PtNi/C-acid, and PtNi/C-acid/heat.

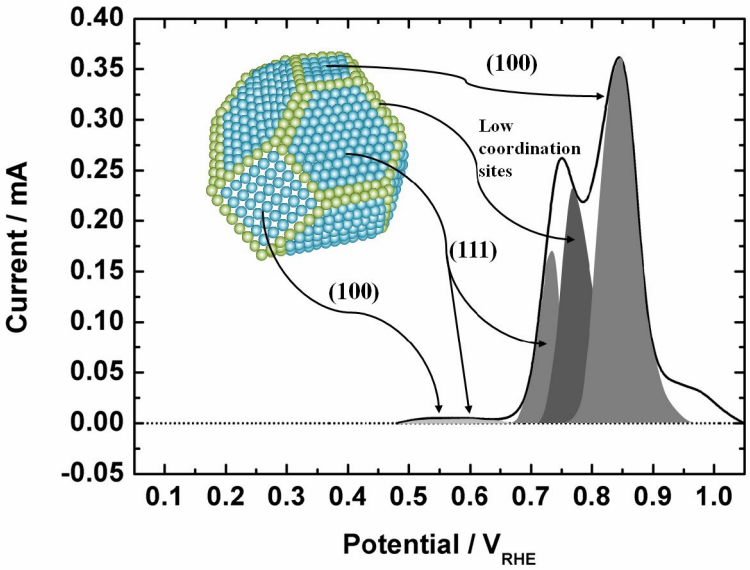

Fig. 3.3 Schematic representation that summarizes the four CO oxidation current peaks and assigns them to specific surface domains and sites.

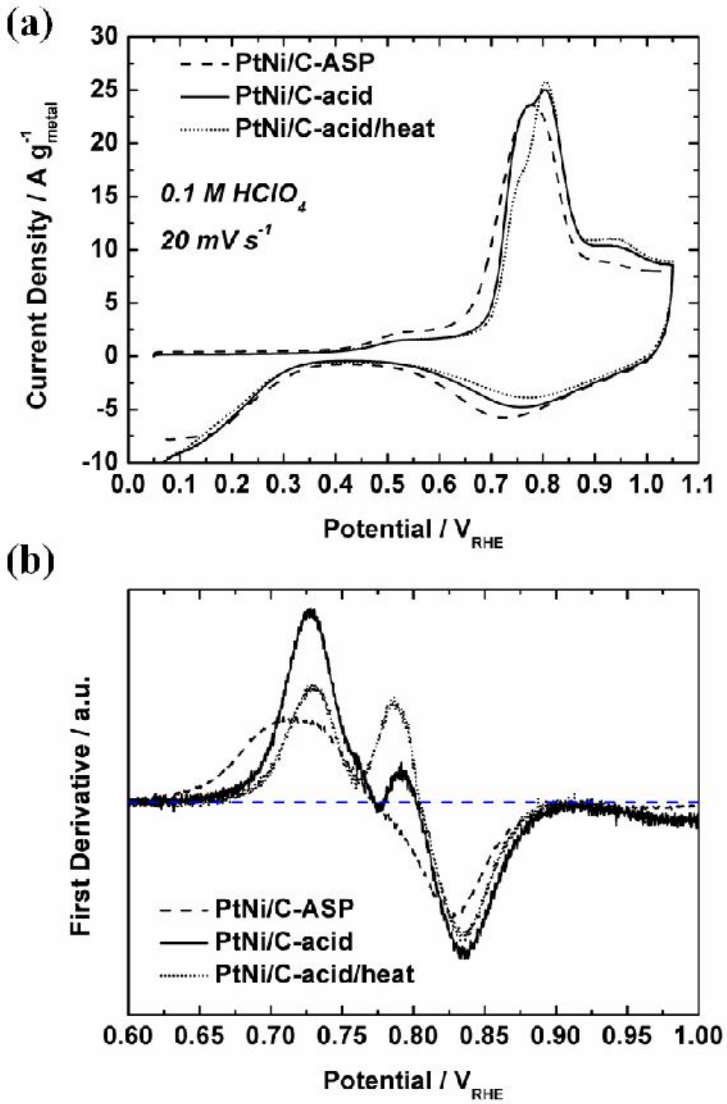

Fig. 3.4 (a) CO oxidation currents and (b) first derivative of CO oxidation currents of PtNi/C-ASP, PtNi/C-acid, and PtNi/C-acid/heat.

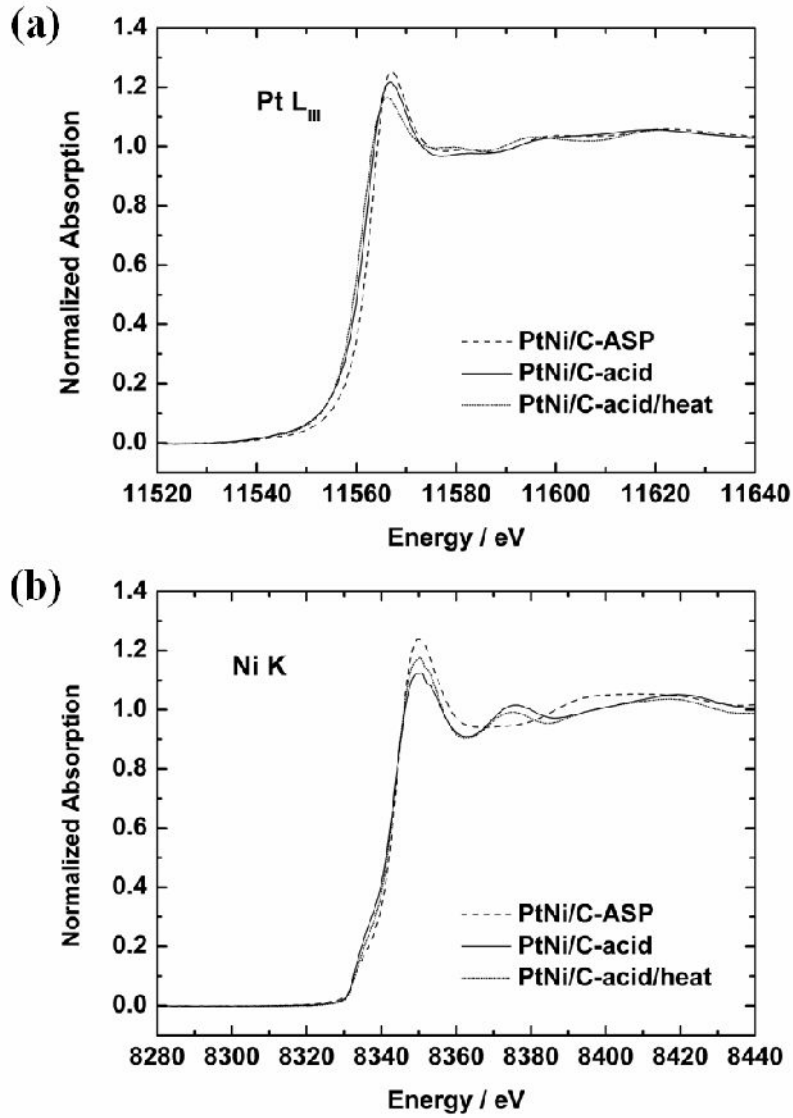

Fig. 3.5 XANES spectra of (a) Pt L_{III} edge and (b) Ni K edge for PtNi/C-ASP, PtNi/C-acid, and PtNi/C-acid/heat.

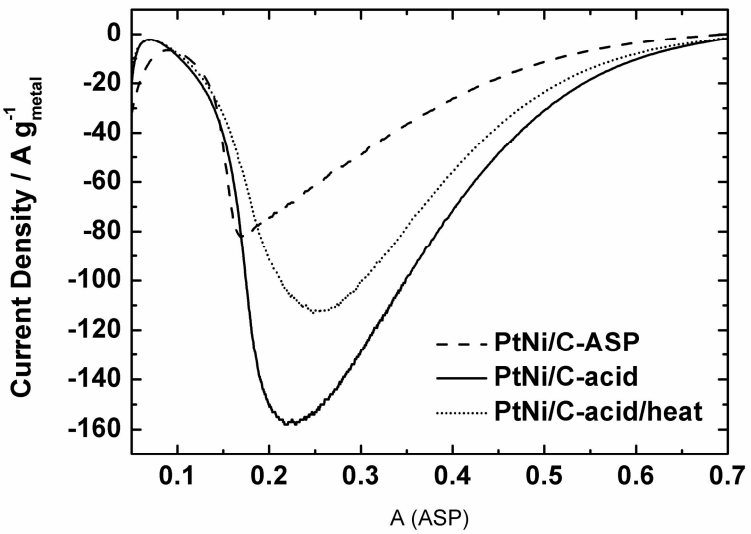

Fig. 3.6 N_2O reduction currents for PtNi/C-ASP, PtNi/C-acid, and PtNi/C-acid/heat.

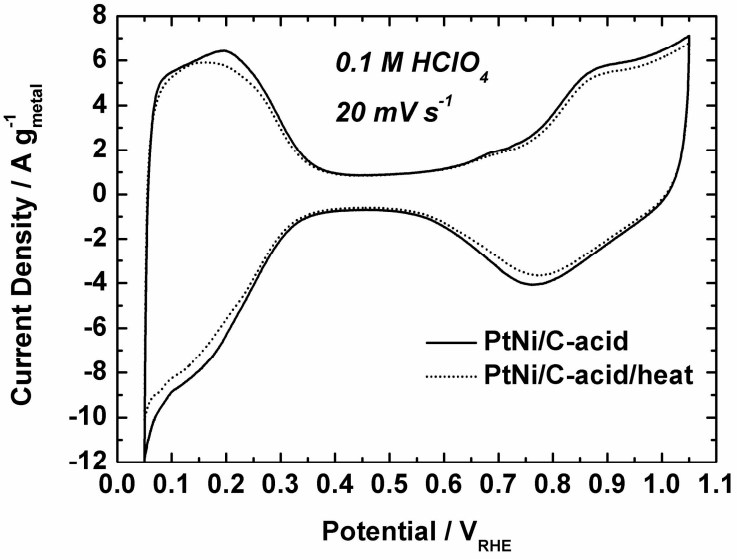

Fig. 3.7 CVs of PtNi/C-acid and PtNi/C-acid heat in 0.1 M $HClO_4$.

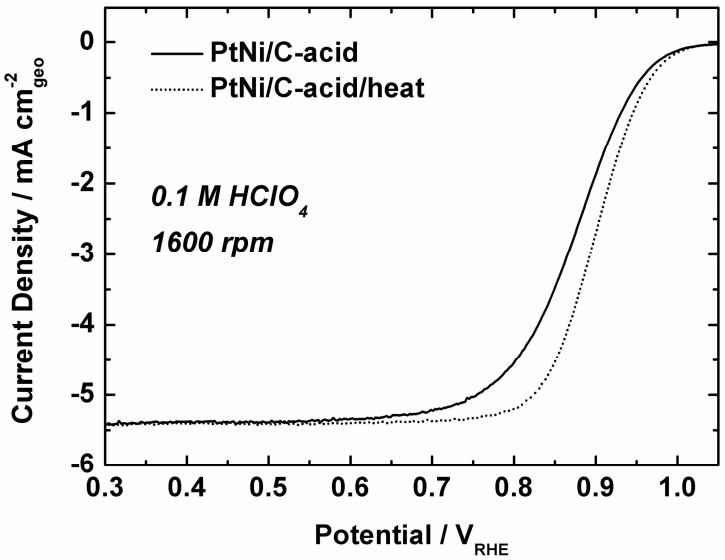

Fig. 3.8 ORR curves for PtNi/C-acid and PtNi/C-acid/heat in 0.1 M $HClO_4$.

3.1.2. Effects of de-alloyed PtNi catalyst on Pt overlayer

Many researchers have been studied the core-shell structure for the enhanced ORR activity in PEMFC. In general, they were mainly concentrated on the chemical compositions of core and shell materials as a core-shell design strategy. However, the surface structure of the core material was one of the most key factors to make the catalytic activity of the shell material changed. Recently, P. Strasser *et al.* elucidated that the Pt-rich shell in the de-alloyed core-shell catalyst exhibited the compressive strain, which resulted in the downshift of the electronic band structure of Pt and weakening the chemisorptions of oxygenated species [9]. It was attributed to the compressive lattice-strain of Pt sublayer by alloying the transition metal. So then, when Pt is overlayered on de-alloyed core-shell, it is considered that the effect of the surface morphology becomes more critical rather than that of the chemical composition on catalytic activity. From this study, the surface structure-induced strain effects of catalysts on the electrochemical property and catalytic activity in PEMFC were investigated.

As shown in Fig. 3.9 and 3.10, Pt@PtNi/C-acid and Pt@PtNi/C-acid/heat had similar particle size and distribution on the carbon support. The average particle size of Pt@PtNi/C-acid and Pt@PtNi/C-acid/heat were 2.6 and 2.8 nm, respectively, which were calculated by Scherrer equation in (220) peak of XRD in Fig. 3.11 and Table 3.2. Different particle size of two samples was attributed to the different particle size of

core materials (PtNi/C-acid : 2.4 nm, PtNi/C-acid-heat : 2.6 nm). When Pt of 7 wt.% was additionally deposited on PtNi/C-acid and PtNi/C-acid/heat, respectively, the thickness of Pt overlayer can be estimated by following equation [10, 11]:

$$D_{Pt@PtNi} = D_{PtNi} \{ 1 + [Pt]\ V_{m,Pt} / [PtNi] (V_{m,Pt}\ \theta_{Pt} + V_{m,Ni}\ \theta_{Ni}) \}^{1/3} \quad (3\text{-}1)$$

Here, V_m is the molar volume; [ ] is the atomic ratio between Pt and PtNi; $D_{Pt@PtNi}$ is the diameter of Pt@PtNi/C-acid or Pt@PtNi/C-acid/heat; D_{PtNi} is the diameter of PtNi/C-acid or PtNi/C-acid/heat; and θ is the atomic fraction between Pt and Ni (here, θ_{Pt} = 0.75 and θ_{Ni} = 0.25 in PtNi/C-acid or PtNi/C-acid/heat due to Pt : Ni = 3 : 1 in Table 3.1). The experimental values of $D_{Pt@PtNi}$ correspond closely to the theoretical values. Accordingly, the thickness of Pt overlayer on PtNi/C-acid and PtNi/C-acid/heat are ~0.2 nm, respectively. However, the atomic ratio of Pt : Ni was 5.8 : 1 from the ICP-AES in Table 3.2, while the calculated values of atomic ratio in two samples were Pt : Ni = 4.2 : 1, This error may be attributed to the analysis procedure, but it can be roughly accepted because the two samples had the same composition in the ICP-AES.

As mentioned in the former section, the CO oxidation peak of PtNi/C-acid started to be slightly separated into near-(111) and (100) facets, and that of PtNi/C-acid/heat was divided further more. It resulted in the

change of the surface and electronic structure. Here, the Pt overlayer with thickness of 0.2 nm was additionally deposited on PtNi/C-acid and PtNi/C-acid/heat to study the strain effects induced from the surface structure of core materials. When Pt was overlayered on PtNi/C-acid/heat with the smooth surface, a long-range ordered (111) facet was fabricated on the surface. As shown in Fig. 3.12, the first CO oxidation peak, which was related to the (111) facet, of Pt@PtNi/C-acid/heat was appeared at below 0.75 V, and two peaks were distinctly indicated compared to PtNi/C-acid/heat. Most of low coordinated Pt atoms on PtNi/C-acid/heat were removed, and stable (111) facet with long-range was formed. In case of Pt@PtNi/C-acid, ordered (111) facet was more developed compared to PtNi/C-acid as a core material since Pt could be nucleated at unstable Pt atoms with low coordination number in the Pt overlayer synthesis. However, it seems that the long-range (111) facet of Pt@PtNi/C-acid could not be formed as that of smooth Pt@PtNi/C-acid/heat because Pt deposition was started from the corrugated surface of PtNi/C-acid. The first CO oxidation peak of Pt@PtNi/C-acid was appeared at 0.75 V, which was more positive potential compared to that of Pt@PtNi/C-acid/heat (0.74 V). It can be clearly identified in Fig. 3.12b. It may be attributed to many vicinal facet between (111) and (100) in Pt@PtNi/C-acid as shown in Fig. 3.3. It is considered that the short-range (111) facets were formed with relatively many boundaries between the (111) and (100) facets on Pt@PtNi/C-acid, which resulted in slightly positive shift of the CO oxidation peak at ~0.75 V. It was expected that this critical

structural difference between Pt@PtNi/C-acid and Pt@PtNi/C-acid/heat could give a new insight about surface structure-induced strain effects. Huang *et al.* studied the surface atom contractions on (111) and (100) facets [12]. In molecular dynamics, the atoms on the vicinal facets between (111) and (100) have a large magnitude of contraction. Therefore, it was considered that Pt@PtNi/C-acid with many vicinal facets between (111) and (100) could be affected by the surface atom contraction much more than Pt@PtNi/C-acid/heat. In addition, Lee et al. hypothesized that the (111) and (100) terrace sizes greatly influence the ORR activity although they could not directly prove the hypothesis [13].

The surface structure-induced compressive strain was also confirmed from the XANSE measurements. As shown in Fig. 3.13, Pt@PtNi/C-acid/heat showed higher white line absorption peak than Pt@PtNi/C-acid in the region of Pt L_{III} XANES although it had well-ordered structure and high coordination number. In addition, in the region of Ni K XANES, Pt@PtNi/C-acid had lower white lie absorption peak compared to Pt@PtNi/C-acid/heat. If the charge transfer was occurred from Ni to Pt, the white line absorption of Ni K XANE in Pt@PtNi/C-acid might be increased. However, the tendency of Pt L_{III} and Ni K XANE was the same in two samples, which ensured the effect of the surface contraction in Pt@PtNi/C-acid. Therefore, the *d*-band center of Pt@PtNi/C-acid could be shifted down from the Fermi-level. In addition, the PZTC was measured to definitely confirm the structure-induced compressive strain on surface Pt. As shown in Fig. 3.14, Pt@PtNi/C-acid showed higher

PZTC and work function than Pt@PtNi/C-acid/heat, and the result corresponded to the downshift of *d*-band center of Pt.

In the CV in Fig. 3.15, the onset potential of Pt oxidation was positively shifted, and the Pt reduction peak was also anodically moved in Pt@PtNi/C-acid due to the decreased in the binding energy between Pt and oxygenated species. Consequently, by the surface structure-induced compressive strain, the half-wave potential of Pt@PtNi/C-acid was higher than that of Pt@PtNi/C-acid/heat in the ORR curves in Fig. 3.16. While surface Pt on Pt@PtNi/C-acid/heat had less compressive strain by the long range-ordered substrate surface, that on Pt@PtNi/C-acid could obtain more compressive strain due to the vicinal facets between (111) and (100) produced on the corrugated substrate material. It is well known that the highest ORR activity is shown on (111) facet rather than (100) facet in $HClO_4$ [14]. However, it is considered that the range of (111) facet is also important due to the surface contraction on the low coordination sites between (111) and (100) of the nanoparticle. Consequently, the study about the Pt overlayer on substrate materials with different surface structure could help understanding the enhancement of the ORR activity by the surface structure-induced strain.

Table 3.2 Physical properties of Pt@PtNi/C-acid and Pt@PtNi/C-acid/heat obtained from ICP-AES, EA, and XRD.

	Pt@PtNi/C-acid	Pt@PtNi/C-acid/heat
Wt.%	37	37
Atomic Ratio (Pt : Ni)	5.8: 1 (theory 4.2 :1)	5.8: 1 (theory 4.2 :1)
Weight Ratio (Pt : Ni)	19.3 : 1 (theory 14 : 1)	19.3 : 1 (theory 14 : 1)
Particle Size (nm)	2.6	2.8
Lattice Parameter (nm)	0.3856	0.3860

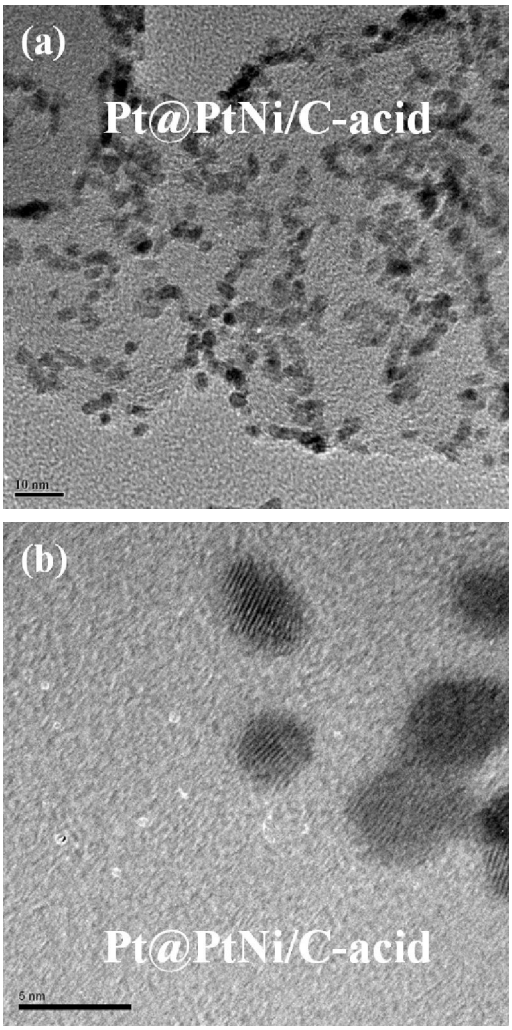

Fig. 3.9 TEM images of Pt@PtNi/C-acid with (a) low magnification and (b) high magnification.

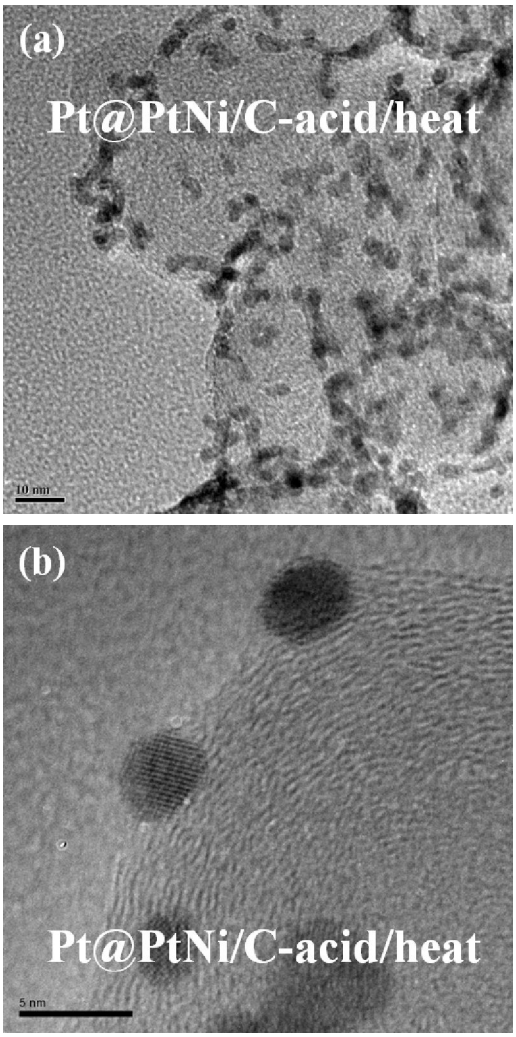

Fig. 3.10 TEM images of Pt@PtNi/C-acid with (a) low magnification and (b) high magnification.

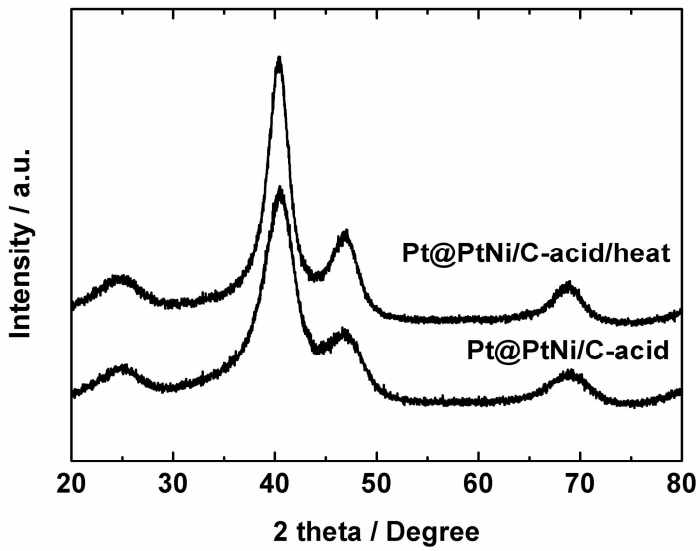

Fig. 3.11 XRD patterns of Pt@PtNi/C-acid and Pt@PtNi/C-acid/heat.

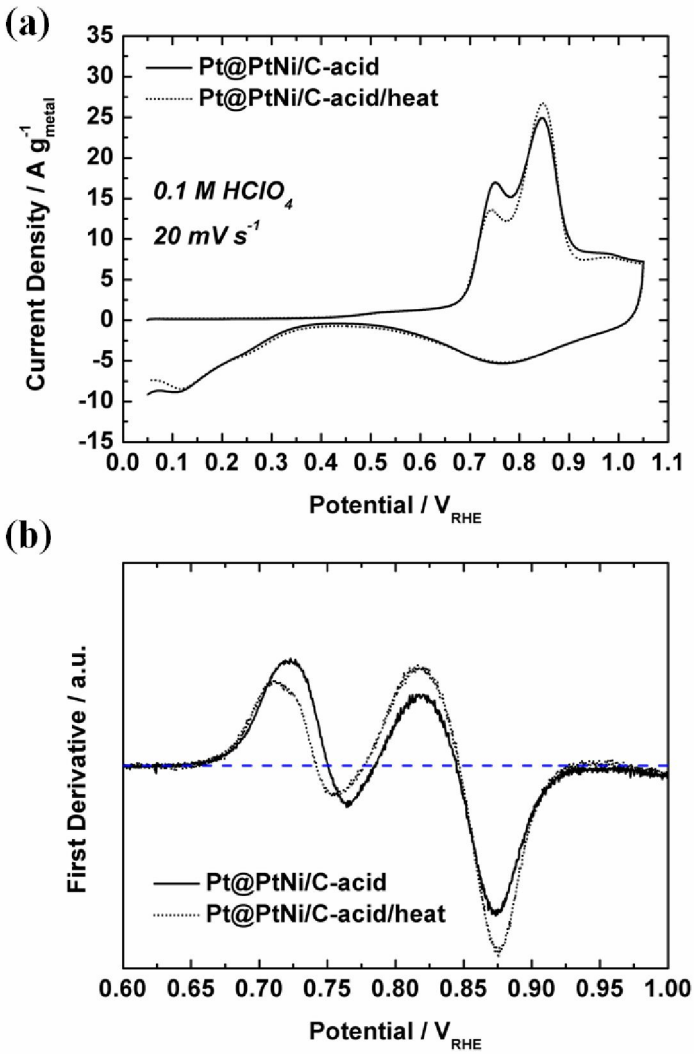

Fig. 3.12 (a) CO oxidation currents and (b) first derivative of CO oxidation currents of Pt@PtNi/C-acid and Pt@PtNi/C-acid/heat.

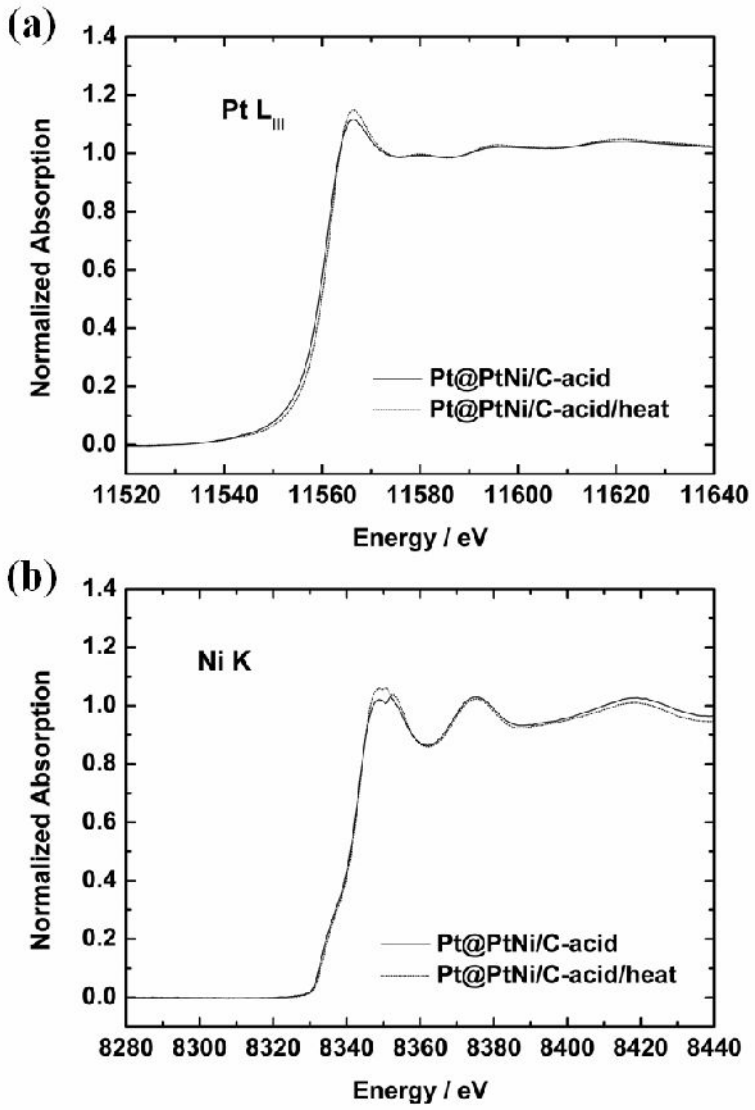

Fig. 3.13 XANES spectra of (a) Pt L_{III} edge and (b) Ni K edge for Pt@PtNi/C-acid and Pt@PtNi/C-acid/heat.

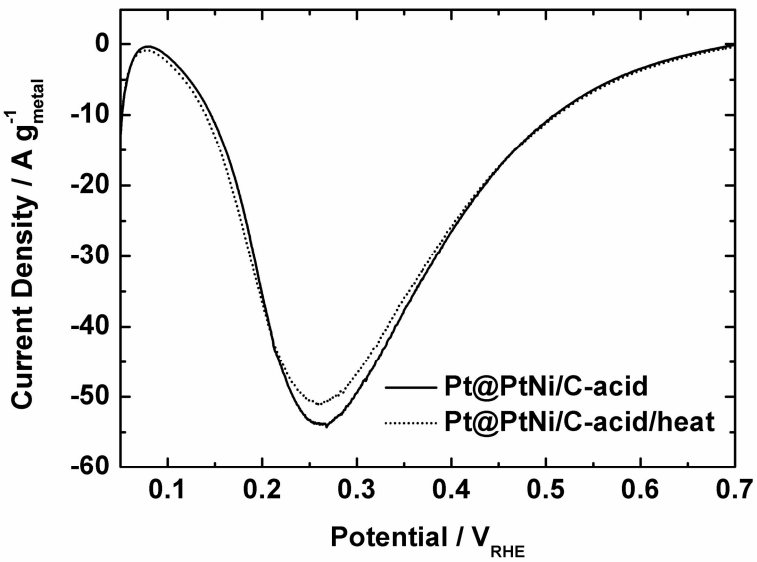

Fig. 3.14 N_2O reduction currents for Pt@PtNi/C-acid and Pt@PtNi/C-acid/heat.

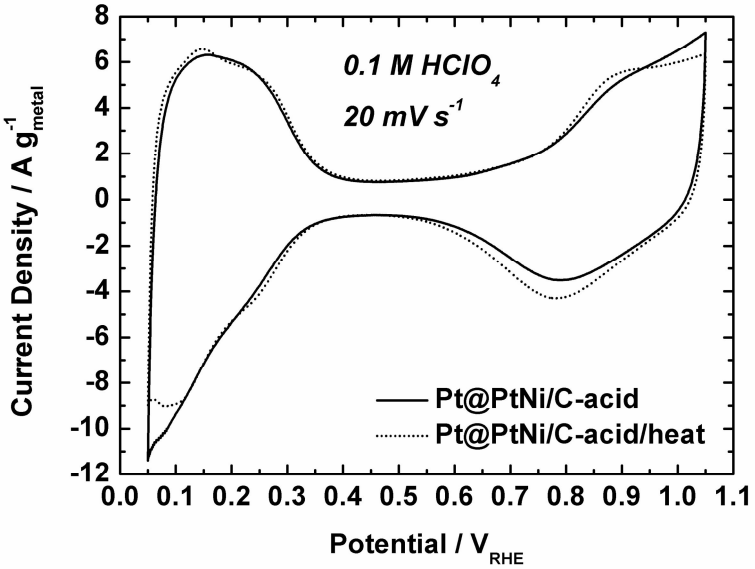

Fig. 3.15 CVs of Pt@PtNi/C-acid and Pt@PtNi/C-acid heat in 0.1 M $HClO_4$.

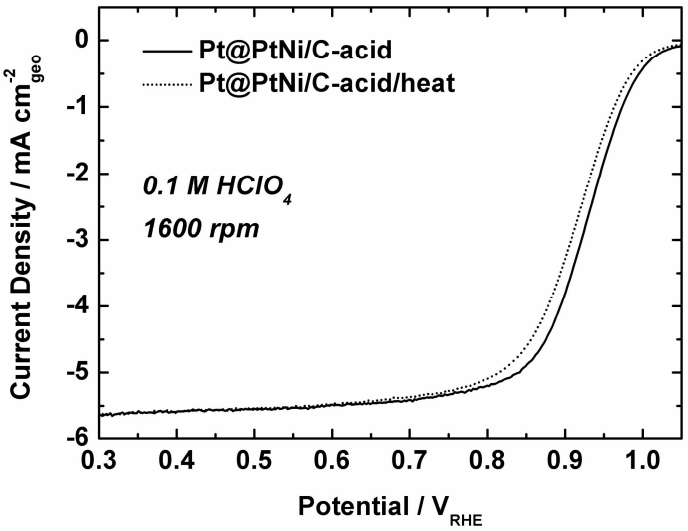

Fig. 3.16 ORR curves for Pt@PtNi/C-acid and Pt@PtNi/C-acid/heat in 0.1 M $HClO_4$.

3.2. Effects of carbon surface modification

3.2.1. Selective functionalization of carbon support

To enhance the water transport in the MEA, a facile way of reducing water flooding in the cathode catalyst layer was proposed through the introduction of carbon-supported Pt (Pt/C) catalyst selectively functionalized by poly(*N*-isopropylacrylamide) (PNIPAM), which is able to reversibly switch between hydrophilic and hydrophobic property depending on the temperature [15]. With this method, one can achieve a hydrophobic catalyst layer without a decrease in the EAS and an increase in the catalyst layer thickness. It is meaningful to selectively functionalize the carbon surface in the existence of metal nanoparticle on the carbon support in PEMFC.

This study has been motivated by the fact that the hydrophilicity needs to be switched at two steps: (i) particle dispersion at MEA preparation process and (ii) water management at PEMFC operation. Namely, the carbon support should have sufficiently high hydrophilic functional groups to uniformly disperse the catalyst of nanoparticles on the carbon surface when carbon supported Pt-based or other metal catalyst is synthesized [16, 17]. Therefore, the carbon support such as carbon black, carbon nanotube (CNT) and carbon nanofiber (CNF) is generally activated through the acid treatment so as to have the functional groups such as -COOH, -C=O and -C-O on the surface, and the hydrophilic

functional groups on carbon still remain after the catalyst synthesis. It is noted in this regard that a catalyst ink having a carbon support without such functional groups have shown bad dispersion [17, 18] and large catalyst agglomerates may be formed in a catalyst layer, which results in low Pt utilization in the MEA [19]. Therefore, the carbon surface needs to be hydrophilic to well disperse the catalyst ink at room temperature, which consists of catalyst, ionomer and solvent. In sharp contrast, from the water management point of view in the MEA, a hydrophobic carbon surface is required to prevent from flooding of the catalyst layer when operating PEMFC at ~70 ℃ since otherwise water can be accumulated on the carbon surface. In addition, oxygen gas can easily transport to the Pt through the hydrophobic channel on the carbon surface [20]. Accordingly, to meet such a wide variation of hydrophilicity from the catalyst synthesis to the PEMFC operation, the wetting property of the carbon surface should be tuned at each step. Two approaches are conceivable at this stage. First, the Pt surface should be intact throughout the carbon surface functionalization. Otherwise, a significant reduction in the active area of Pt nanoparticles would occur. Second, a material with temperature-directed switchable hydrophilicity is needed because a variable is only the temperature from room temperature (catalyst ink preparation) to ~70 ℃ (PEMFC operation).

It is known that PNIPAM exhibits thermally responsive switching between hydrophilicity and hydrophobicity [21-26]. This phenomenon is explained by the competition between intermolecular and intermolecular

hydrogen bonding below and above the lower critical solution temperature (LCST) of ~32 ℃. Owing to this excellent responsive behaviour, PNIPAM has been studied in broad research areas, such as tissue engineering, drug delivery, and micro/nano actuators after being tailored to respond to a specific stimulus. Herein, we utilize the switchable wetting of PNIPAM in PEMFC by selective functionalization in order to tackle the above challenge, i.e., spontaneous wetting transition from hydrophilic to hydrophobic without deteriorating the active area of the catalyst. Fig. 3.17 shows a schematic illustration for the synthesis of selectively-functionalized Pt/C (Pt/C-PNIPAM). Here, amine-terminated PNIPAM (NH_2-PNIPAM) and functional groups (-COOH) on the carbon surface selectively formed the amide (-CONH) bond with the aid of 1-ethyl-3-(3-dimethylaminopropyl)carbodiimide (EDC) as a catalyst [27]. Subsequently, reactant residue was eliminated through the filtration by excessive D.I. water. This chemical synthetic mechanism can give selectivity for the functionalization of the carbon surface despite the existence of Pt nanoparticles.

As shown in Fig. 3.18, The catalyst layer thickness with Pt/C-PNIPAM (4.9 μm) was similar to that with Pt/C (5.0 μm). Moreover, there is no isolated polymer particle in the catalyst layer with Pt/C-PNIPAM. It shows that PNIPAM did not agglomerate each other, and it may be located only on catalyst surfaces with well-dispersed. The catalysts were properly agglomerated each other in the catalyst layer of the MEAs as shown in Fig. 3.19. It means that Pt/C-PNIPAM was well mixed in the

catalyst ink since PNIPAM was hydrophilic at room temperature during the MEA preparation. Interestingly, the surface of Pt/C-PNIPAM seemed similar to that of non-treated Pt/C in the scanning electron microscope (SEM) images. To identify the surface structure of the catalysts, the surface roughness of Pt/C and Pt/C-PNIPAM was additionally measured by AFM. From the analysis, it was observed that the surface of Pt/C-PNIPAM was rougher than the Pt/C surface, with the measured roughnesses being 9.44 nm and 15.00 nm for Pt/C and Pt/C-PNIPAM, respectively. It shows that PNIPAM can be well distributed among Pt nanoparticles on the carbon surface.

For the characterization of the amide formation, each catalyst surface was analyzed by XPS. The existence of N 1s peak at 400.5 eV of Pt/C-PNIPAM shows that PNIPAM was definitely located on Pt/C, and the amide bond was formed between the carbon surface and PNIPAM [28, 29]. (Fig. 3.20) In addition, it was confirmed that PNIPAM was selectively functionalized only on the carbon surfaces without affecting Pt surfaces. Fig. 3.21a indicates that Pt 4f core-level peaks of Pt/C and Pt/C-PNIPAM were hardly changed, and the ratio of Pt oxidation states of Pt/C-PNIPAM was analogous to that of Pt/C. (Fig. 3.22 and Table 3.3) Especially, cyclic voltammograms (CV) of the cathode catalyst layers with and without PNIPAM were also similar to each other, and the EAS of Pt/C-PNIPAM calculated from the H_{upd} regions was comparable to that of Pt/C as shown in Fig. 21b. Based on these observations, it was concluded that PNIPAM did not attach to Pt nanoparticles, and hardly

affected the electronic structure of Pt catalyst. Therefore, the synthetic method for carbon surface functionalization secured the selectivity. In addition, it was identified from XRD patterns in Fig. 3.23 that Pt crystalline of Pt/C-PNIPAM was not affected in catalyst preparation since the diffraction patterns of two samples were not changed.

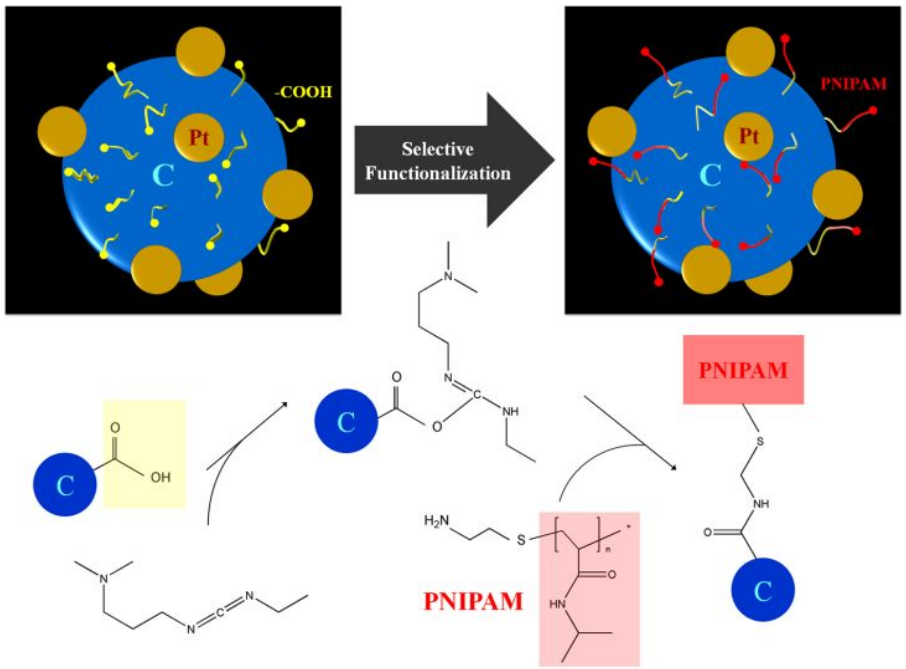

Fig. 3.17 Schematic illustration of synthesis of selectively-functionalized Pt/C (Pt/C-PNIPAM).

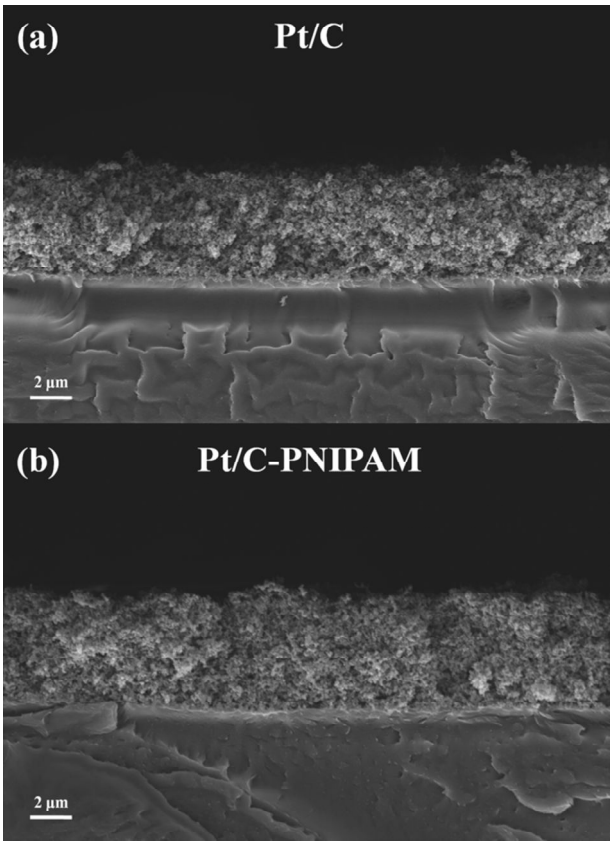

Fig. 3.18 SEM images showing the catalyst layer thickness of (a) Pt/C (~4.9 μm) and (b) Pt/C-PNIPAM (~5.0 μm).

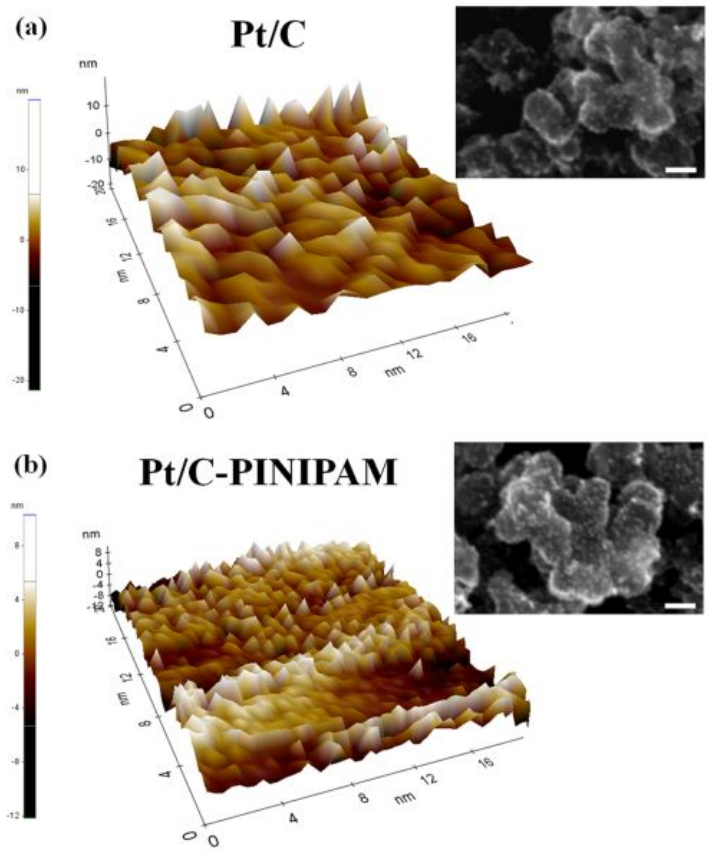

Fig. 3.19 AFM images showing the morphology of each surface: (a) Pt/C, (b) Pt/C-PNIPAM. Each inset shows corresponding SEM images. (Scale bar: 50 nm)

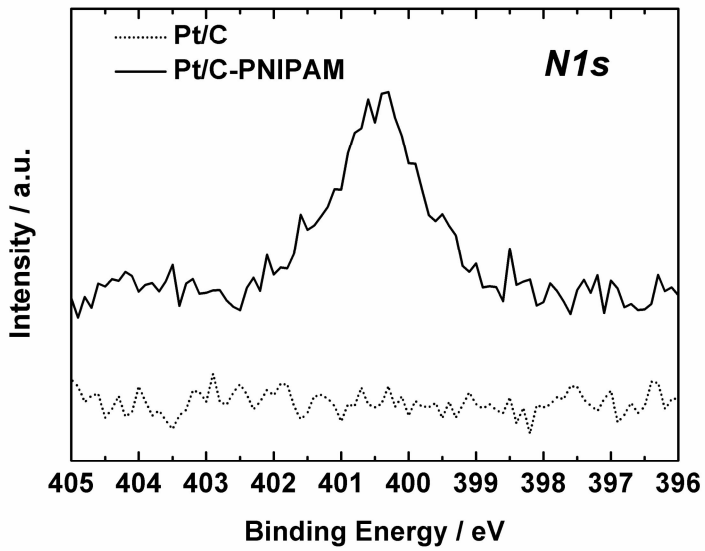

Fig. 3.20 XPS peaks of N1s for Pt/C and Pt/C-PNIPAM.

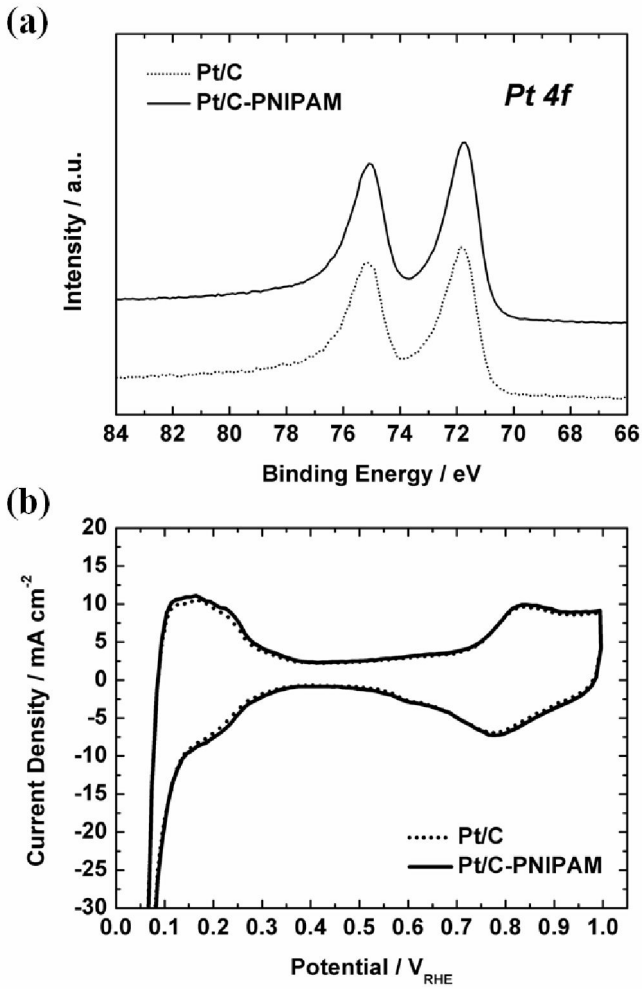

Fig. 3.21 (a) XPS peaks of Pt4f and (b) CVs for Pt/C and Pt/C-PNIPAM.

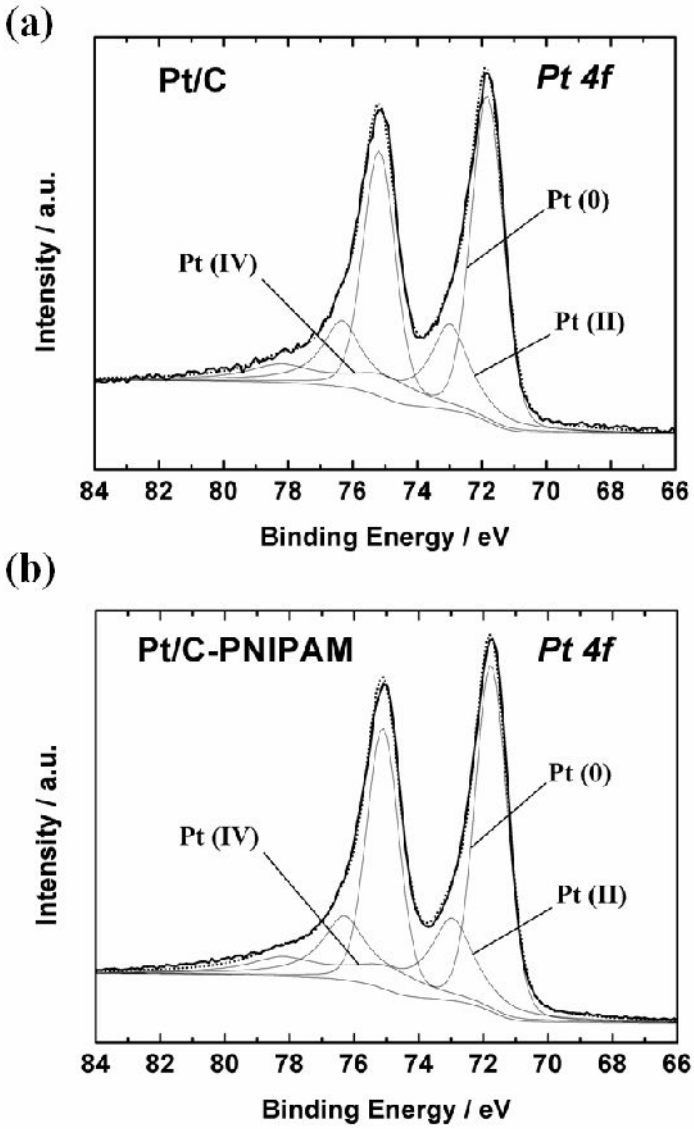

Fig. 3.22 Deconvolution for XPS peaks of Pt4f of (a) Pt/C and (b) Pt/C-PNIPAM.

Table 3.3 Atomic ratio of Pt oxidation states of Pt/C and Pt/C-PNIPAM.

Material	Element	Oxidation State	Binding Energy [eV]	Ratio [%]
Pt/C	Pt 4f	Pt (0)	71.2	62.2
		Pt (II)	72.3	29
		Pt (IV)	74.6	8.8
Pt/C-PNIPAM	Pt 4f	Pt (0)	71.2	61.9
		Pt (II)	72.4	29.2
		Pt (IV)	74.6	8.9

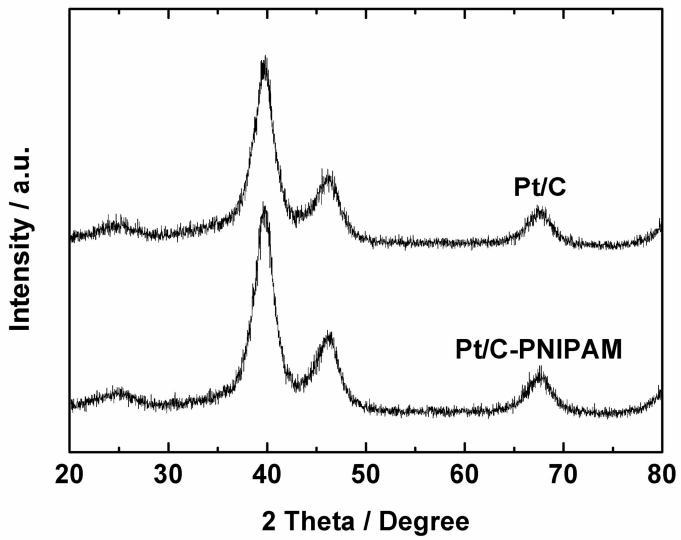

Fig. 3.23 XRD patterns for Pt/C and Pt/C-PNIPAM.

3.2.2. Thermal responsibility of modified carbon surface

Thermal responsibility of PNIPAM on the carbon surface was verified by measuring advancing and receding contact angles (CAs) at ~20 ℃ (below LCST) and ~70 ℃ (above LCST) as shown in Fig. 3.24 and Table 3.4. Large and small values of CA hysteresis show the hydrophilic and hydrophobic surface properties, respectively. The catalyst layers with Pt/C had similar and high CA hysteresis (= θ_a-θ_r) at 20℃ and 70 ℃. It means that Pt/C may have strong water retention ability in the catalyst layer regardless of the PEMFC operating temperature. On the contrary, Pt/C-PNIPAM showed a CA hysteresis of ~5.2 at 70 ℃, suggesting that the catalyst layer with Pt/C-PNIPAM is very hydrophobic when operating a PEMFC at 70 ℃. It is noted in this regard that the CA hysteresis turned out to be the most critical factor to ensure optimal performance of PEMFC for the water management [30, 31].

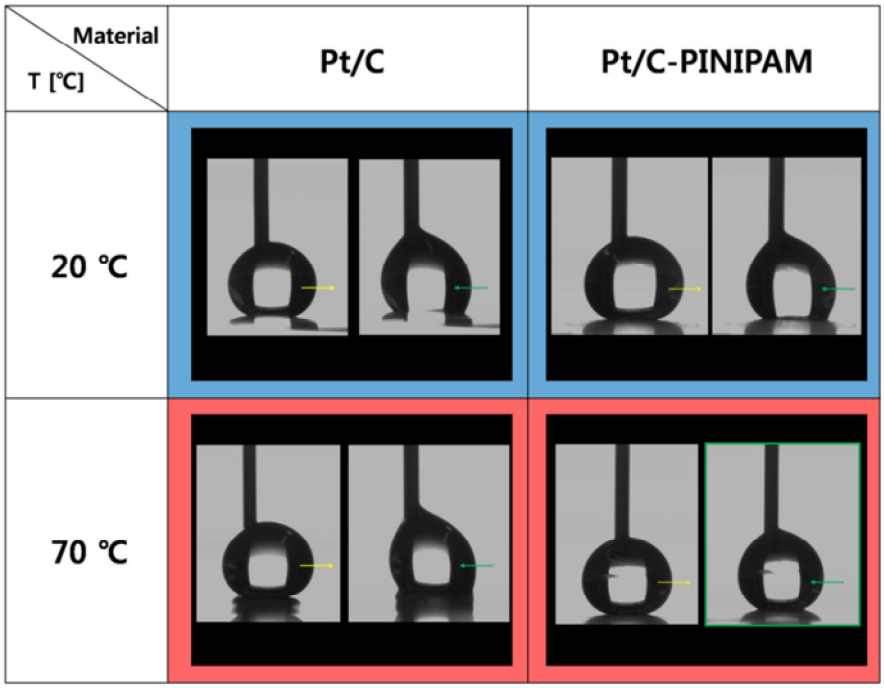

Fig. 3.24 Photographs of advancing and receding contact angles depending on temperature and surface material.

Table 3.4 Contact angle (static, advancing and receding) data depending on temperature and surface composing materials. Hysteresis in the adhesion energy was calculated based on the data.

Material	Temperature, T [℃]	Contact angle, θ [°]	Advancing contact angle, θa [°]	Receding contact angle, θr [°]	ΔAdhesion energy, ΔW [mJ/m2]
Pt/C	20	148.2	149.9	122.3	24.1
	70	144.1	147.8	125.2	19.6
Pt/C-PNIPAM	20	149.5	150.6	121.9	25
	70	148.7	151.8	146.6	3.4

3.2.3. Enhanced water transport in cathode of PEMFC

As shown in Fig. 3.25, the MEA using Pt/C-PNIPAM as a cathode catalyst showed a distinctively higher unit cell performance than that using Pt/C at 70 ℃. Interestingly, PNIPAM on the carbon surface affected the fuel cell performance mainly in the high current region related to water flooding. This means that the MEA with Pt/C-PNIPAM may have a high power density in the high current region, since water flooding was reduced by hydrophobic property of PNIPAM-functionalized carbon surface. The PEMFC performance in the low current region, however, was nearly the same as that of Pt/C since Pt catalyst of Pt/C-PNIPAM was not affected by the selective functionalization of the carbon support. Additionally, the semi- circles in the low frequency region of the electrochemical impedance spectroscopy (EIS) in Fig. 3.26 indicated that the mass transfer resistance of Pt/C-PNIPAM was smaller to that of Pt/C. When the EIS data was fitted and calculated by the equivalent circuit in Fig. 2.2, the Warbug impedance of Pt/C-PNIPAM (0.055 Ohm cm^2) was much smaller than that of Pt/C (0.085 Ohm cm^2) although the current density Pt/C-PNIPAM was higher than that of Pt/C at 0.65 V. It means that the removal rate of water from Pt/C-PNIPAM was increased, and oxygen could rapidly access to the Pt catalyst through the hydrophobic carbon surface.

To understand the enhanced water transport in the catalyst layer with Pt/C-PNIPAM, we propose here a simple theoretical model. We

hypothesize that the systematic pressure and adhesion force at the solid-liquid interface would compete each other as the driving force (F_d) and the resistant force (F_r), respectively, and thus might determine the extent of water transported through pores in the MEA. The MEA surfaces of Pt/C and Pt/C-PNIPAM are highly hydrophobic as can be seen from the CAs in Table 3.4. Hence, the pressure difference (ΔP) should overcome the Laplace pressure (ΔP_L) to force water into pores [32]. The relation is expressed in a simple form, given by

$$F_d \geq \Delta P_L \cdot A = (2\gamma_w |\cos\theta|)/r_p \cdot (\pi r_p^2) = \pi\gamma_w r_p |\cos\theta|, (\theta \geq 90) \qquad (3\text{-}2)$$

where γ_w is the surface tension of water, r_p is the average radius of pore and θ is the CA of pore surface.

When considering the counterbalancing term, water transport is inhibited by adhesion or retention of water on pore surface. The difference in the adhesion energy (ΔW) at the solid-liquid interface can be calculated by measuring the CA hysteresis [30, 33, 34]. Accordingly, the resistant force of water transport can be obtained as

$$F_r = \Delta W \cdot l = \gamma_w (\cos\theta_r - \cos\theta_a) \cdot (2\pi r_p) \qquad (3\text{-}3)$$

where θ_r is the receding CA and θ_a is the advancing CA.

To set up an index to determine efficient water transport, the ratio of F_d to F_r can be used, i.e.,

$$F_d/F_r \geq (|\cos\theta|)/(\cos\theta_r - \cos\theta_a) \quad (3\text{-}4)$$

For the conditions used in our experiment, the ratios are 3.0 and 18.4 for Pt/C and Pt/C-PNIPAM, respectively, suggesting that the latter allows for a much higher driving force for water transport. It further indicates that Pt/C-PNIPAM could easily remove water from the carbon surface in the catalyst layer. A detailed kinetic model incorporating the role of three phase interactions is currently under investigation.

In summary, Pt/C catalyst was selectively functionalized by thermally responsive PNIPAM to reversibly switch the wetting properties of the carbon surface from hydrophilic to hydrophobic. During the MEA fabrication and PEMFC operation, Pt/C-PNIPAM was able to change its surface property with respective to its operation temperature. Notably, the Pt catalyst was not affected by the surface functionalization; it was well mixed in the catalyst ink at room temperature, and showed consistent unit cell performance in the low current density region without affecting Pt catalyst in the PEMFC operation. In the high current density region, by contrast, hydrophobic property of Pt/C-PNIPAM caused the power density to increase significantly due to fast removal of water and rapid oxygen accessibility to the Pt surface in the catalyst layer. Consequently, it was confirmed that selective functionalization of the carbon support with thermally responsive polymer was successful for the water management in PEMFC. In addition, it is envisioned that the present

synthetic idea and experimental results may provide a new insight for various energy device applications using organic and inorganic composite materials and functional polymers.

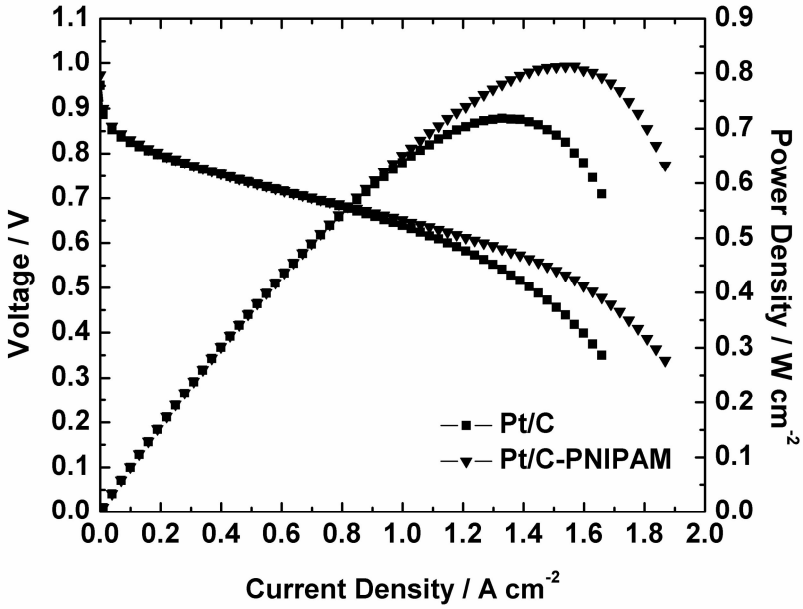

Fig. 3.25 Unit cell performance of MEAs with Pt/C and Pt/C-PNIPAM.

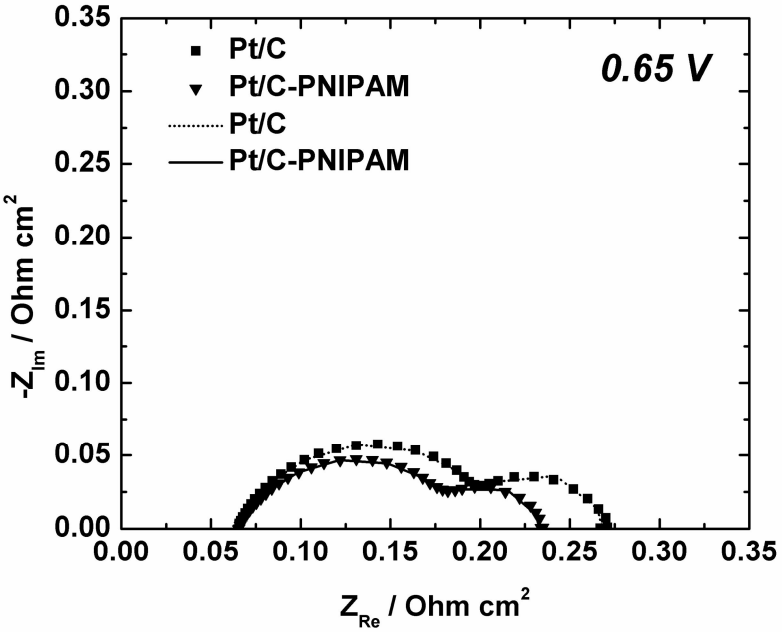

Fig. 3.26 EIS of MEAs with Pt/C and Pt/C-PNIPAM. (Dot: raw data, Line: fitting data)

3.3. References

1. C. Wang, M. Chi, D. Li, D. Strmcnik, D. Vliet, G. Wang, V. Komanicky, K.-C. Chang, A. P. Paulikas, D. Tripkovic, J. Pearson, K. L. More, N. M. Markovic, V. R. Stamenkovic, "Design and synthesis of bimetallic electrocatalyst with multilayered Pt-skin surfaces", *J. Am. Chem. Soc.* **2011**, 133, 14396.

2. P. Urchaga, S. Baranton, C. Coutanceau, G. Jerkiewicz, "Electro-oxidation of COchem on Pt Nanosurfaces: Solution of the Peak Multiplicity Puzzle", *Langmuir* **2012**, 28, 3658.

3. N. M. Marković, C. A. Lucas, B. N. Grgur, P. N. Ross, "Surface electrochemistry of CO and H_2/CO mixtures at Pt(100) interface: electrode kinetics and interfacial structures", *J. Phys. Chem. B* **1999**, 103, 9616.

4. B. Hammer, O.H. Nielsen, J.K. Nørskov, "Structure sensitivity in adsorption: CO interaction with stepped and reconstructed Pt surfaces", *Catal. Lett.* **1997**, 46, 31.

5. T.-Y. Jeon, S. J. Yoo, Y.-H. Cho, K.-S. Lee, S. H. Kang, Y.-E. Sung, "Influence of oxide on the oxygen reduction reaction of carbon-supported Pt?Ni alloy nanoparticles", *J. Phys. Chem. C* **2009**, 113, 19732.

6. T.-Y. Jeon, S. J. Yoo, H.-Y. Park, S.-K. Kim, S. Lim, D. Peck, D.-H. Jung, Y.-E. Sung, "Electrocatalytic effects of carbon dissolution in Pd nanoparticles", *Langmuir* **2012**, 28, 3664.

7. B. Hammer, Y. Morikawa, J. K. Nørskov, "CO Chemisorption at metal surfaces and overlayers", *Phys. Rev. Lett.* **1996**, 76, 2141.

8. V. R. Stamenkovic, B. S. Mun, M. Arenz, K. J. J. Mayrhofer, C. A. Lucas, G. Wang, P. N. Ross, N. M. Markovic, "Trends in electrocatalysis on extended and nanoscale Pt-bimetallic alloy surfaces", *Nature Mater.* **2007**, 6, 241.

9. P. Strasser, S. Koh, T. Anniyev, J. Greeley, K. More, C. Yu, Z. Liu, S. Kaya, D. Nordlund, H. Ogasawar, M. F. Toney, A. Nilsson, "Lattice-strain control of the activity in dealloyed core–shell fuel cell catalysts", *Nature Chem.* **2010**, 2, 454.

10. D. Zhao, B.-Q. Xu, "Enhancement of Pt utilization in electrocatalysts by using gold nanoparticles", *Angew. chem. Int. Ed.* **2006**, 45, 4955.

11. K.-S. Lee, I.-S. Park, H.-Y. Park, T.-Y. Jeon, Y.-H. Cho, Y.-E. Sung, "PtRu-modified Au nanoparticles as electrocatalysts for direct methanol fuel cells", *J. Electrochem. Soc.* **2009**, 156, B1150.

12. W. J. Huang, R. Sun, J. Tao, L. D. Menard, R. G. Nuzzo, J. M. Zuo, "Coordination-dependent surface atomic contraction in nanocrystals revealed by coherent diffraction", *Nature Mater.* **2008**, 7, 308.

13. S. W. Lee, S. Chen, J. Suntivich, K. Sasaki, R. R. Adzic, Y. Shao-Horn, "Role of surface steps of Pt nanoparticles on the electrochemical activity for oxygen reduction", *J. Phys. Chem. Lett.* **2010**, 1, 1316.

14. N. Markovic, H. Gasteiger, P. N. Ross, "Kinetics of oxygen reduction on Pt(hkl) electrodes: implications for the crystallite size effect with supported Pt electrocatalysts", *J. Electrochem. Soc.* **1997**, 144, 1591.

15. T. Sun, G. Wang, L. Feng, B. Liu, Y. Ma, L. Jiang, D. Zhu, "Reversible switching between superhydrophilicity and superhydrophobicity", *Angew.*

Chem. Int. Ed. **2004**, 43, 357.

16. X. Yua, S. Ye, "Recent advances in activity and durability enhancement of Pt/C catalytic cathode in PEMFC: Part II: Degradation mechanism and durability enhancement of carbon supported platinum catalyst", *J. Power Sources* **2007**, 172, 145.

17. Y. Xing, "Synthesis and electrochemical characterization of uniformly-dispersed high loading Pt nanoparticles on sonochemically-treated carbon nanotubes", *J. Phys. Chem. B* **2004**, 108, 19255.

18. J. Chena, Q. Chena, Q. Ma, "Influence of surface functionalization via chemical oxidation on the properties of carbon nanotubes", *J. Colloid Interf. Sci.* **2012**, 370, 32.

19. N. Jung, Y.-H. Cho, K.-H. Choi, J. W. Lim, Y.-H. Cho, M. Ahn, Y. S. Kang, Y.-E. Sung, "Preparation process for improving cathode electrode structure in direct methanol fuel cell", *Electrochem. Commun.* **2010**, 12, 754.

20. R. Friedmann, T. V. Nguyen, "Optimization of the microstructure of the cathode catalyst layer of a PEMFC for two-phase flow", *J. Electrochem. Soc.* **2010**, 157, B260.

21. H. Tekin, T. Tsinman, J. G. Sanchez, B. J. Jones, G. Camci-Unal, J. W. Nichol, R. Langer, A. Khademhosseini, "Responsive micromolds for sequential patterning of hydrogel microstructures", *J. Am. Chem. Soc.* **2011**, 133, 12944.

22. M. Ebara, M. Yamato, T. Aoyagi, A. Kikuchi, K. Sakai, T. Okano, "Temperature-responsive cell culture surfaces enable “On−Off” affinity

control between cell integrins and RGDS ligands", *Biomacromolecules* **2004**, 5, 505.

23. G. Huang, J. Gao, Z. Hu, J. V St. John, B. C Ponder, D. Moro, "Controlled drug release from hydrogel nanoparticle networks", *J. Control. Release* **2004**, 94, 303.

24. S. Zhua, C. Chen, Z. Chen, X. Liu, Y. Li, Y. Shi, D. Zhang,"Thermo-responsive polymer-functionalized mesoporous carbon for controlled drug release", *Mater. Chem. Phys.* **2011**, 126, 357.

25. X. Zhang, C. L. Pint, M. H. Lee, B. E. Schubert, A. Jamshidi, K. Takei, H. Ko, A. Gillies, R. Bardhan, J. J. Urban, M. Wu, R. Fearing, A. Javey, "Optically- and thermally-responsive programmable materials based on carbon nanotube-hydrogel polymer composites", *Nano Lett.* **2011**, 11, 3239.

26. N. I. Abu-Laila, M. Kaholeka, B. LaMattinac, R. L. Clarka, S. Zauscher, "Micro-cantilevers with end-grafted stimulus-responsive polymer brushes for actuation and sensing", *Sensor. Actuat. B-Chem.* **2006**, 114, 371.

27. N. Nakajima, Y. Ikada, "Mechanism of amide formation by carbodiimide for bioconjugation in aqueous media", *Bioconjugate Chem.* **1995**, 6, 123.

28. B. Ruelle, S. Peeterbroeck, R. Gouttebaron, T. Godfroid, F. Monteverde, J.-P. Dauchot, M. Alexandre, M. Hecq, P. Dubois, "Functionalization of carbon nanotubes by atomic nitrogen formed in a microwave plasma Ar + N2 and subsequent poly(ε-caprolactone) grafting", *J. Mater. Chem.* **2007**, 17, 157.

29. Q. Peng, X. He, Y. Li, C. Wang, R. Wang, P. Hu, Y. Yan, T. Sritharan,

"Chemically and uniformly grafting carbon nanotubes onto carbon fibers by poly(amidoamine) for enhancing interfacial strength in carbon fiber composites", *J. Mater. Chem.* **2012**, 22, 5928.

30. E. Chibowski, "Surface free energy of a solid from contact angle hysteresis", *Adv. Colloid Interfac.* **2003**, 103, 149.

31. Y. Rahmawan, M.-W. Moon, K.-S. Kim, K.-R. Lee, K.-Y. Suh, "Wrinkled, dual-scale structures of diamond-like carbon (DLC) for superhydrophobicity", *Langmuir* **2010**, 26, 484.

32. J. Benziger, J. Nehlsen, D. Blackwell, T. Brennan, J. Itescu, "Water flow in the gas diffusion layer of PEM fuel cells", *J. Membrane Sci.* **2005**, 261, 98.

33. J. N. Israelachvili, Intermolecular and surface forces, Academic press, **2011**.

34. T. Kim, K. Y. Suh, "Unidirectional wetting and spreading on stooped polymer nanohairs", *Soft Matter* **2009**, 5, 4131.

Chapter 4. Conclusions

In PEMFC, the sluggish cathode reaction and water flooding considerably affects the charge transfer resistance for the ORR and mass transfer resistance related to water produced by the ORR, respectively, in the cathode. Large overpotnetials by these resistances are the main reason of the fuel cell performance degradation, and they are attributed definitely to the catalysts. O_2 should be rapidly reduced to water on metal nanoparticles of the catalyst, but water produced by the ORR has to be removed from the catalyst surface. This situation makes difficult requirements for the cathode catalyst design in PEMFC. Nevertheless, the most important thing is that all kinds of electrochemical reaction including the ORR are occurred on the surface, and the water retention and removal also results from the surface property. Accordingly, the surface of metal nanoparticle and carbon support composed of fuel cell catalysts were modified via various methods to enhance the ORR activity and water transport, respectively, in the cathode of PEMFC. In addition, understanding the electrochemical and physical meaning was intensively pursued.

The surface structure modification of PtNi/C-ASP was started through de-alloying by the acid and heat treatment. This strategy to change the catalyst surface structure has been well known. Corrugated “Pt-skeleton” structure (PtNi/C-acid) was attributed to leaching out surface Ni atoms by the acid treatment, and the “Pt-skin” structure (PtNi/C-acid/heat) was fabricated due to smoothing the surface Pt atoms on “Pt-skeleton” structure by heating.

However, the rational explanation how the surface smoothing was conducted was not enough to understand the enhancement of the ORR activity in PtNi/C with “Pt-skin” structure. In this thesis, the surface smoothing process was electrochemically confirmed by CO stripping current measurements, and it was investigated that the surface structure on the catalyst affected the Pt electronic structure. PtNi/C-ASP showed very broad CO oxidation peak because it had a highly disordered surface structure. However, the CO oxidation peak of PtNi/C-acid was started to be gradually separated. In addition, two distinct CO oxidation peaks were formed in PtNi/C-acid/heat, and moved into the direction of peak potentials for the stable (100) and (111) facets. By the XANES and PZTC measurement, it was confirmed that PtNi/C-acid/heat had high coordination number and work function. Therefore, the downshift of *d*-band center of surface Pt in PtNi/C-acid/heat resulted in a decrease in the binding energy between Pt and oxygenated species and an increase in the ORR activity.

Based on above results, the effect of surface structure in catalysts was intensively studied. Pt overlayers were additionally deposited on PtNi/C-acid and PtNi/C-acid/heat, which were Pt@PtNi/C-acid and PtNi/C-acid/heat, respectively. By different surface structures of PtNi/C-acid and PtNi/C-acid/heat as substrate materials, the surface structure of additional surface Pt atoms was definitely affected. The CO oxidation current peaks in both pt@PtNi/C-acid and Pt@PtNi/C-acid/heat were more clearly separated, but the range of (111) facet formation was different according to the surface structure of substrate materials. Pt@PtNi/C-acid fabricated with corrugated

PtNi/C-acid had more short-range (111) facets with many boundaries between (111) and (100) facets while Pt@PtNi/C-acid/heat had long-range (111) facets. However, at the low coordination sites at the boundary, surface atom contraction (surface strain) was occurred in Pt@PtNi/C-acid. By the surface structure-induced strain, the white line absorption peaks of Pt@PtNi/C-acid were decreased in the XANES region, and Pt@PtNi/C-acid could have high work function. On the contrary, Pt@PtNi/C-acid/heat with too much stable long-range (111) facet did not obtain the surface strains due to high coordination number of the substrate material. Consequently, the study about the Pt overlayer on substrate materials with different surface structure could help understanding the enhancement of the ORR activity by the surface structure-induced strain.

Finally, a new strategy to enhance the water transport on catalyst surface was proposed through the surface modification of carbon support in Pt/C catalyst. It is required to change the surface property of carbon since water produced by the ORR on fuel cell catalyst is accumulated on the surface of carbon support. Hydrophilic carbon is needed to load metal nanoparticles as catalysts on carbon support, and the hydrophilic property of carbon support is necessary because the carbon-supported catalyst should be well dispersed in the catalyst ink when the MEA fabricated. However, if the carbon support of Pt/C is hydrophobic, it can take advantages for the water transport on carbon surface in the PEMFC operation. Accordingly, the hydrophilicity of carbon needs to be switched at each step: particle dispersion at ~20 °C in the MEA preparation process and water management at ~70 °C in the PEMFC

operation. To meet the difficult requirements, the carbon with self-switchable hydrophilicity is definitely required, and the carbon surface modification should not affect the surface of Pt nanoparticles on the carbon support not to lose the catalytic activity. Therefore, a thermally responsive PNIPAM was selected as a surface tuning material on carbon. Additionally, for the selective funtionalization of carbon surface, amine- terminated NH_2-PNIPAM was used eventually for the amide reaction between NH_2- and -COOH on carbon surface. The selective functionalization of PNIPAM was proved by the XPS and CV measurement. The existence of N 1s core level peak in Pt/C-PNIPAM and no change of Pt 4f core level peaks and CVs in both Pt/C and Pt/C-PNIPAM clearly ensured the selective funtionalization. In addition, it was confirmed that the thermal responsibility of Pt/C-PNIPAM could be verified by measuring advancing and receding contact angles. The catalyst layers with Pt/C had high contact angle hysteresis at 20°C and 70 °C. It means that Pt/C may have strong water retention ability in the catalyst layer regardless of the PEMFC operating temperature. On the contrary, Pt/C-PNIPAM showed a small contact angle hysteresis at 70 °C, suggesting that the catalyst layer with Pt/C-PNIPAM is very hydrophobic when operating a PEMFC at 70 °C. It is worthwhile noting that the CA hysteresis turned out to be the most critical factor to ensure optimal performance of PEMFC for the water management. Therefore, the MEA with PNIPAM in the cathode catalyst layer was much higher fuel cell performance in the high current density region. In addition, the interfacial relation between the modified carbon and water was understood by a simple

theoretical model.

These surface modifications of catalyst (metal nanoparticle and carbon support) could give significant changes of the electrochemical property and catalytic activity in PEMFC. The changes were also proved by various measurements. Consequently, it was concluded that understanding the surface structure of catalysts was necessarily required for advanced material designs in the electrochemical energy conversion devices.

국 문 초 록

수소 이온 교환 막 연료전지는 미래의 전기화학적 에너지 변환 장치로 큰 잠재력을 가지고 있다. 수소가 가지는 화학에너지를 다른 기계적인 변환 과정 없이 직접적으로 전기발생을 유도함으로써 에너지 변환을 위한 이론 효율이 83 %로 일반적인 내연 기관에 비해 월등히 높다. 그러나 수소 이온 교환 막 연료전지를 상용화하기까지는 아직 해결해야 할 문제들이 많이 남아 있다. 그러한 미해결 과제들은 재료 및 소재 개발, 장치 제조 공정, 운전 조건, 연료 개질, 연료 저장 문제 등과 관련하여 서로 복잡하게 얽혀 있다. 그 중에서도 수소 이온 교환 막 연료전지에서 가장 중요한 요소는 전기화학 반응을 통해 전기를 생산해내는 막전극 접합체이다. 특히, 수소 이온 교환 막 연료전지의 성능을 증대시키기 위한 핵심 부분은 막전극 접합체 내의 환원 전극이라고 할 수 있다.

수소 이온 교환 막 연료전지에서는 가장 큰 두 가지 과전압 손실이 모두 환원 전극으로부터 나온다. 첫 번째 과전압 손실은 낮은 전류 밀도 영역에서 매우 느린 산소 환원 반응으로부터 발생하는 전하 전달 저항과 깊은 관련이 있다. 이러한 전하 전달 저항을 줄이기 위해, PtM (M = Fe, Co, Ni) 합금, 코어−쉘 구조, 입자 형상

제어 등 다양한 금속 나노 입자 개발이 진행되고 있다. 두 번째 과전압 손실은 높은 전류 밀도 영역에서 산소환원 반응을 통해 과량의 물이 발생하여 산소의 접근을 방해하는 환원 전극 홍수 현상 때문에 나타나게 된다. 금속 촉매 입자의 표면에서 산소환원 반응으로 발생한 물이 탄소 지지체의 표면에 축적이 되고, 나아가 촉매-촉매 사이에 물이 고여 전극 내 홍수 현상이 나타나게 된다. 이러한 환원 전극 내 효과적인 물 관리를 위해 소수성을 가진 입자를 전극 내 삽입하거나 기공 형성제를 넣어 큰 기공을 만드는 연구들이 진행되어 왔다. 그러나 많은 노력에도 불구하고 위의 두 가지 과전압 손실은 여전히 수소 이온 교환 막 연료전지의 성능 저하에 상당한 부분을 차지 하고 있다.

금속 나노 입자 위에서의 산소환원 반응과 탄소 지지체에서의 물 축적 문제는 모두 소재의 표면 성질과 직접적인 관련을 가지기 때문에, 촉매 (금속 나노 입자 및 탄소 지지체)의 표면 구조는 그 문제들을 해결하기 위한 핵심 요소가 될 수 있다. 먼저, 높은 산소환원 반응 활성을 위한 환원극 촉매 개발을 위해, 탄소에 담지 된 백금-니켈 합금 촉매 (PtNi/C)를 합성하였고, 금속 나노 입자의 다양한 표면 개질을 통해 그 구조적 영향에 대한 연구를 진행하였다. 산처리를 통해 백금-니켈 합금의 표면에 있는 니켈 원자를 녹여 냄으로써 de-alloying을 유도하였다. 그리고 이렇게 만들어진

de-alloying 된 백금-니켈 합금을 다시 열처리 하여, 니켈 원자가 녹아 나가면서 생성되었던 굴곡진 촉매 입자 표면을 매끄럽게 하였다. 또한 산처리 된 백금-니켈 입자와 산처리와 열처리가 동반된 백금-니켈 입자 위에 다시 백금 층을 올려 코어 물질의 표면 구조가 백금 쉘의 전기화학적 특성 및 산소환원 반응 활성에 미치는 영향을 살펴 보았다. 다양한 표면 구조의 변화는 주로 일산화탄소 산화 전류 측정을 통해 연구 되었고, 그 변화된 표면 구조로 인한 백금 전자 구조의 영향은 X-ray absorption near-edge structure spectroscopy (XANES)와 potential of zero total charge (PZTC)를 통해 확인하였다. 촉매 표면 개질 공정에 따라 (111)과 (100) 결정면의 형성 정도가 다르게 나타났고, 그것은 백금의 전자 구조와 전기화학적 특성을 변화 시켰다. 따라서 백금과 산소종 (oxygen species) 사이의 결합 에너지의 차이가 발생하게 되어 산소 환원 반응의 활성에 뚜렷한 차이를 나타내게 됨을 확인하였다.

물질 전달과 관련 된 두 번째 과전압 손실을 줄이기 위한 시도는, 막전극 접합체의 환원 전극 내 물 이동을 증대시키기 위해 온도에 반응하는 poly(N-isopropylacrylamide) (PNIPAM)을 이용하여 탄소 지지체 표면을 선택적으로 개질하는 방법을 선택하였다. 수소 이온 교환 막 연료전지의 촉매 지지체로서 탄소 입자는 그

표면에 금속 나노 입자를 담지하기 위해서는 여러 탄소 기능기가 필요하기 때문에, 일반적으로 친수성의 표면을 갖는 탄소를 사용하게 된다. 또한 막전극 접합체 제작을 위한 촉매 잉크 제조 시, 탄소에 담지 된 촉매가 나피온 이오노머, 물, 알콜 용매와 잘 혼합되어야 하기 때문에 친수성을 갖는 탄소 입자가 요구된다. 그러나 막전극 접합체를 제조한 후, 실제 연료전지 구동 시 70 ℃ 정도에서 탄소 입자 표면에 물의 축적을 피해야 하므로 반대로 소수성 표면이 필요하게 되는데 앞서 언급한 촉매 및 촉매 잉크 제조 과정 때문에 그 문제를 해결하기 어려운 점이 있었다. 이러한 탄소 지지체의 표면 성질에 대한 문제를 해결하기 위해 온도에 따라 친수성/소수성이 변하는 PNIPAM을 탄소 표면에 선택적으로 결합시켰고, 그 선택적 결합 과정이 산소환원 촉매로 사용되는 백금 나노 입자에는 영향을 거의 주지 않았다. 선택적 탄소 표면 개질은 X-ray photoelectron spectroscopy (XPS)와 순환 전압법을 통해 증명하였고, 20 ℃와 70 ℃에서 물방울의 접촉각 이력현상 (contact angle hysteresis) 측정을 통해 온도에 따른 친수성/소수성의 변화를 확인하였다. 선택적 탄소 표면의 기능화로 인해 상온에서 촉매 잉크 제조 시 촉매의 분산도에 전혀 문제가 없었으며, 70 ℃에서 연료전지 구동 시 막전극 접합체 내 물의 이동 능력 증대로 인해 연료전지 성능이 향상되었다. 또한 개질 된 탄소 표면 성질과 물

이동과의 상관 관계를 이해하기 위해 간단한 이론 모델을 세워 보았다.

결론적으로, 위와 같은 촉매 (금속 나노 입자 및 탄소 지지체)의 표면 구조의 개질을 통해 수소 이온 교환 막 연료전지에서 전기화학적 성질과 촉매 활성의 변화를 유도할 수 있음을 확인하였고, 또한 촉매의 여러 가지 표면 구조에 대한 이해를 바탕으로 전기화학적 에너지 변환 장치에 응용 될 수 있는 소재 개발에 대한 새로운 전략을 얻을 수 있었다.

주요어: 연료전지, 촉매, 탄소, 표면 구조, 산소환원 반응, 물 이동
학 번: 2009-31264